

Lattice Boltzmann modelling of salt precipitation during brine evaporation

Junyu Yang^a, Timan Lei^a, Geng Wang^a, Qianghui Xu^b, Jin Chen^a, Kai H. Luo^{a,*}

^a Department of Mechanical Engineering, University College London, Torrington Place, London WC1E 7JE, United Kingdom

^b School of Mechanical Engineering, Beijing Institute of Technology, Beijing 100081, China



ARTICLE INFO

Keywords:

Salt precipitation
Brine evaporation
Pore-scale modelling
Lattice Boltzmann method
Classical nucleation theory

ABSTRACT

Salt precipitation during brine evaporation in porous media is an important phenomenon in a variety of natural and engineering scenarios. This work establishes a multiphase multicomponent lattice Boltzmann (LB) method with phase change for simulating salt precipitation during brine evaporation. In the proposed LB models, the gas-brine multiphase flow, brine evaporation, salt concentration evolution, salt precipitate nucleation and growth are simultaneously considered. Simulations of the Stefan problem are first conducted to verify the proposed numerical models and determine the diffusion coefficient of brine vapour. Once the lattice Boltzmann models have been validated, salt precipitation during brine evaporation is simulated to investigate the competition mechanisms between salt precipitate nucleation and growth reaction. The results show that the typical salt precipitation patterns in existing experimental observation can be successfully reproduced, including the ring-like and pancake-like patterns. The difference in the salt precipitation patterns is explained by the competition mechanism between precipitate growth and nucleation according to the present study. Furthermore, the salt precipitation during gas injection into a microfluidic chip is investigated. The evolution of salt and brine saturation shows similar patterns to existing experimental results, and the effects of the gas injection rate on salt precipitation performance are clarified. The LB models in the present work can simulate salt precipitation with comprehensive consideration of multiphase brine evaporation, salt species mass transport, precipitate nucleation and growth, which have not been realized in previous studies. The numerical showcases demonstrate the excellent performance of the proposed models for the simulation of salt precipitation in porous media, which promise to guide practical engineering applications like CO₂ sequestration.

1. Introduction

Salt precipitation during brine evaporation in porous media can be found in numerous natural and industrial processes, including soil salinization (Han et al., 2022; Nachshon et al., 2011; Shokri-Kuehni et al., 2020; Zhaoyong et al., 2014), drying of building materials (Espinosa-Marzial and Scherer, 2010, 2022; Flatt et al., 2014; Fonseca and Scherer, 2014) and carbon dioxide (CO₂) geological sequestration (Borgia et al., 2012; Fujii and Kawasaki, 2019; Oh et al., 2013; Ott et al., 2015; Sokama-Neuyam et al., 2019; Tambach et al., 2014; Zhang and Wang, 2012). In the case of CO₂ sequestration, for example (He et al., 2019), when dry CO₂ is injected into deep saline formations, water evaporated from brine is continually carried away by the gas, resulting in the increasing salt concentration. Once the salt concentration reaches the supersaturation state, the nucleation and growth of salt precipitate start. The accumulated salt precipitate alters the pore structure and transport properties of the reservoir formations, which can impair the

injectivity, sealing, and storage capacity of CO₂ sequestration (Ho and Tsai, 2020). In these situations, multiphysics processes, including gas-brine multiphase flow, brine evaporation, advection and diffusion of salt in brine, nucleation and growth of salt precipitates, are strongly coupled in porous media, determining the salt precipitation behaviours on the macroscopic scales. Thus, understanding these multiphysics processes at the pore scale is a prerequisite to finding measures that limit salt precipitation damage.

In recent years, a wide range of pore-scale experiments including two-dimensional microfluidics (He et al., 2019, 2022; Ho and Tsai, 2020; Kim et al., 2013; Miri et al., 2015) and three-dimensional X-ray micro-computed tomography (micro-CT) (Akindipe et al., 2021, 2022; Norouzi Rad et al., 2013; Ott et al., 2015; Rad et al., 2015; Roels et al., 2014; Shokri, 2014) have been performed to identify the characteristics of salt precipitation. These experimental investigations provided insights into the morphological evolution patterns of salt precipitation during gas injection and brine evaporation, shedding light on the

* Corresponding author.

E-mail address: k.luo@ucl.ac.uk (K.H. Luo).

regulation of salt precipitation. However, the phenomena observed in the experiments are still limited. Some in-depth physical mechanisms such as the evolution of salt concentration cannot be captured. In order to gain a more comprehensive and quantitative understanding based on the experimental phenomena, pore-scale numerical simulations that can fully reveal the reaction and transport mechanisms in porous media are necessary. Recently, various pore-scale numerical methods have been developed to simulate multiphysical processes (Kohanpur et al., 2020; Saxena et al., 2017; Yang et al., 2016), including micro-continuum approach (Deng et al., 2022a), pore-network models (Dashtian et al., 2018), and lattice Boltzmann (LB) method (Prasianakis et al., 2017). Thanks to its promising parallel scalability and convenient boundary treatment (Latt et al., 2021), the LB method has a huge potential for pore-scale simulations, including the simulation of salt precipitation in porous media.

Simulating salt precipitation during brine evaporation with the LB method is challenging considering the following three major issues to be addressed: (1) Gas–brine multiphase flow involving brine evaporation and mass transfer of brine vapour in the gas phase; (2) mass transfer of salt solute in brine and salt concentration increase due to the brine evaporation; (3) nucleation and growth kinetics of salt precipitation. In order to resolve these issues, the development of corresponding numerical models is required. With respect to gas–brine multiphase flow, a series of multiphase LB models have been proposed for years based on the colour-gradient model (Gunstensen et al., 1991), the pseudopotential model (Shan and Chen, 1993), the free energy model (Swift et al., 1996) and the phase-field model (He et al., 1999). Among these models, the pseudopotential model's simplicity of programming and broad adaptability have led to its widespread application in simulating complex physical phenomena, including bubble dynamics (Peng et al., 2019) and phase change (Zhou et al., 2019). It is also appropriate for modelling gas–brine multiphase flow during salt precipitation. In the pseudopotential model, phase separation is achieved on the basis of two kinds of interaction forces between the particle distributions, i.e., intercomponent and intracomponent interaction forces (Mukherjee et al., 2019). By adopting the intracomponent force, the equation of state (EOS) for a single component is introduced to separate the vapour and liquid phase, allowing for the simulation of fluid evaporation. The intercomponent force is used to separate different fluid components such as gas and brine. The combination of these two forces allows for the simulation of gas–brine multiphase flow and brine evaporation. Shortly after the pseudopotential model was proposed, Shan and Doolen (1995) pointed out that the model has the capability to simulate mass transfer of different fluid components considering intercomponent diffusion. Guo et al. (2022) derived the specific formula for the diffusion coefficient with Chapman–Enskog analysis and applied the pseudopotential model to simulate mass transfer around the rising bubble. Therefore, the pseudopotential model is able to address issue (1) by simulating multiphase flow, phase change and intercomponent mass transfer simultaneously. On the other hand, one of the challenges here is that the explicit calculation of the diffusion coefficients is too complicated. Moreover, there remains the question of how to set the diffusivity of each fluid component conveniently in the simulation.

For the aforementioned issue (2), the widely used advection–diffusion LB algorithm (Flekkoy, 1993; Sullivan et al., 2005) is suitable for simulating the mass transfer of salt species in brine. The problem is how to calculate salt concentration rise due to evaporation at the gas–brine interface. As reviewed in our previous work (Yang et al., 2022), there are three main kinds of LB models for solute mass transfer in the multiphase system, including the lattice-interface-tracking scheme, physical-interface-tracking scheme and phase-fraction-indicating scheme. The primary point in simulating the evaporation-induced salt concentration rise at the interface is to ensure salt mass conservation at the interface. Since the first two models require the capture of the phase interface position, the mass conservation at the interface is difficult to guarantee in complex multi-phase systems

involving large deformations of the interface shape. The phase-fraction-indicating scheme, which introduces the interfacial mass transfer by calculating the local phase fraction gradients, enables the simulation of the concentration jump at the phase interface with mass conservation. Therefore, the phase-fraction-indicating scheme is more suitable for simulating salt concentration rise at the gas–brine interface. Based on the continuum species transfer (CST) theory, our previous work proposed a phase-fraction-indicating scheme called CST-LB model (Yang et al., 2021). This method has been verified to accurately simulate interfacial mass transfer in complex multiphase flow systems, but its ability to calculate the solute concentration evolution in only one phase during phase change still requires further validation.

Regarding the final issue (3), several attempts have been made to simulate salt precipitation nucleation and growth within LB frameworks (Chen et al., 2014; Fazeli et al., 2020; Prasianakis et al., 2017; Yoon et al., 2012). The precipitation growth is typically described by chemical reaction while the implementation of nucleation has progressed from the direct use of concentration threshold (Chen et al., 2014) to the application of classical nucleation theory (CNT) (Fazeli et al., 2020; Prasianakis et al., 2017). These studies underscore the necessity of incorporating nucleation processes into numerical models, as exclusive precipitation growth modelling fails to accurately replicate observed conditions. In simulating nucleation processes, the CNT is predominantly utilized in numerical models currently, owing to its comprehensive consideration of key parameters such as supersaturation and interfacial free energy that influence nucleation rates. It has demonstrated success in accurately replicating the precipitation growth process observed in nature. Prasianakis et al. (2017) introduced CNT to calculate nucleation kinetics and subsequent precipitation growth based on the concentration field obtained from LB modelling. They compared numerical and experimental results and revealed effects of homogeneous and heterogeneous nucleation. Starchenko (2022) employed CNT to simulate mineral nucleation and growth under varied regimes, thereby illustrating the intricate interaction among reactive transport, chemical reactions, and nucleation phenomena. Although the CNT can accurately forecast the kinetics of nucleation, it lacks the ability to predict the location of nucleation. This limitation arises because mineral nucleation is a probabilistic process, allowing for the possibility of precipitates nucleating anywhere under comparable conditions (Nooraeipour et al., 2021b). To account for the random nature of nucleation in the simulation, Fazeli et al. (2020) proposed a novel probabilistic model based on CNT to investigate salt precipitation performance under different supersaturations, growth rates, and flow rates in both two-dimensional (Fazeli et al., 2020; Nooraeipour et al., 2021a) and three-dimensional porous media (Masoudi et al., 2021). By incorporating normally distributed random numbers, they were able to calculate nucleation induction time, effectively estimating the frequency of nucleation events within a specified time interval. Inspired by this model, Deng et al. (2022b) further investigated the dynamics of interface-coupled dissolution-precipitation processes. These investigations demonstrate the capacity of CNT to calculate salt precipitation nucleation kinetics, providing a solution to issue (3). Note that the previous numerical work is usually carried out in the single-phase scenario. The interplay between nucleation kinetics and multiphase flow patterns should be considered comprehensively when introducing CNT into the simulation of evaporation-induced salt precipitation.

In summary, the existing numerical models are expected to solve the three major issues albeit with further refinements and validations. However, to the best of our knowledge, pore-scale numerical models that fully couple brine evaporation, salt solute mass transfer, and salt precipitation processes have not been achieved. In the present work, numerical models based on the lattice Boltzmann method are proposed to simulate the salt precipitation during the brine evaporation process, considering gas–brine multiphase flow with brine evaporation, salt species mass transfer in brine, salt precipitate nucleation and growth kinetics. Some benchmarks of numerical applications are also performed

to verify the numerical performance of the proposed models and obtain a preliminary understanding of salt precipitation mechanisms.

2. Numerical models

In this section, the numerical models will be introduced to simulate salt precipitation during brine evaporation. We first introduce the pseudopotential model for multiphase gas–brine flow with phase change. A strategy is proposed to set the numerical parameter for the diffusion coefficient of the vapour component in the gas phase. The

$$\mathbf{e}_\alpha = \begin{bmatrix} 0 & 1 & -1 & 0 & 0 & 0 & 1 & -1 & 1 & -1 & 1 & -1 & 1 & -1 & 0 & 0 & 0 & 0 \\ 0 & 0 & 0 & 1 & -1 & 0 & 0 & 1 & 1 & -1 & -1 & 0 & 0 & 0 & 1 & -1 & 1 & -1 \\ 0 & 0 & 0 & 0 & 0 & 1 & -1 & 0 & 0 & 0 & 0 & 1 & 1 & -1 & -1 & 1 & -1 & -1 \end{bmatrix} \quad (2)$$

$$\mathbf{M} = \begin{bmatrix} 1 & 1 & 1 & 1 & 1 & 1 & 1 & 1 & 1 & 1 & 1 & 1 & 1 & 1 & 1 & 1 & 1 & 1 & 1 \\ -30 & -11 & -11 & -11 & -11 & -11 & -11 & -11 & 8 & 8 & 8 & 8 & 8 & 8 & 8 & 8 & 8 & 8 & 8 \\ 12 & -4 & -4 & -4 & -4 & -4 & -4 & -4 & 1 & 1 & 1 & 1 & 1 & 1 & 1 & 1 & 1 & 1 & 1 \\ 0 & 1 & -1 & 0 & 0 & 0 & 0 & 0 & 1 & -1 & 1 & -1 & 1 & -1 & 1 & -1 & 0 & 0 & 0 \\ 0 & -4 & 4 & 0 & 0 & 0 & 0 & 0 & 1 & -1 & 1 & -1 & 1 & -1 & 1 & -1 & 0 & 0 & 0 \\ 0 & 0 & 0 & 1 & -1 & 0 & 0 & 0 & 1 & 1 & -1 & -1 & 0 & 0 & 0 & 0 & 1 & -1 & 1 \\ 0 & 0 & 0 & -4 & 4 & 0 & 0 & 0 & 1 & 1 & -1 & -1 & 0 & 0 & 0 & 0 & 1 & -1 & 1 \\ 0 & 0 & 0 & 0 & 0 & 1 & -1 & 0 & 0 & 0 & 0 & 1 & 1 & -1 & -1 & 1 & 1 & -1 \\ 0 & 0 & 0 & 0 & -4 & 4 & 0 & 0 & 0 & 0 & 0 & 1 & 1 & -1 & -1 & 1 & 1 & -1 \\ 0 & 2 & 2 & -1 & -1 & -1 & -1 & 1 & 1 & 1 & 1 & 1 & 1 & 1 & 1 & -2 & -2 & -2 & -2 \\ 0 & -4 & -4 & 2 & 2 & 2 & 2 & 1 & 1 & 1 & 1 & 1 & 1 & 1 & 1 & -2 & -2 & -2 & -2 \\ 0 & 0 & 0 & 1 & 1 & -1 & -1 & 1 & 1 & 1 & 1 & -1 & -1 & -1 & -1 & 0 & 0 & 0 & 0 \\ 0 & 0 & 0 & -2 & -2 & 2 & 2 & 1 & 1 & 1 & 1 & -1 & -1 & -1 & -1 & 0 & 0 & 0 & 0 \\ 0 & 0 & 0 & 0 & 0 & 0 & 0 & 1 & -1 & -1 & 1 & 0 & 0 & 0 & 0 & 0 & 0 & 0 & 0 \\ 0 & 0 & 0 & 0 & 0 & 0 & 0 & 0 & 0 & 0 & 0 & 0 & 0 & 0 & 0 & 1 & -1 & -1 & 1 \\ 0 & 0 & 0 & 0 & 0 & 0 & 0 & 0 & 0 & 0 & 0 & 1 & -1 & -1 & 1 & 0 & 0 & 0 & 0 \\ 0 & 0 & 0 & 0 & 0 & 0 & 0 & 1 & -1 & 1 & -1 & -1 & 1 & -1 & 1 & 0 & 0 & 0 & 0 \\ 0 & 0 & 0 & 0 & 0 & 0 & 0 & -1 & -1 & 1 & 1 & 0 & 0 & 0 & 0 & 1 & -1 & 1 & -1 \\ 0 & 0 & 0 & 0 & 0 & 0 & 0 & 0 & 0 & 0 & 0 & 1 & 1 & -1 & -1 & -1 & -1 & 1 & 1 \end{bmatrix} \quad (3)$$

evolution of salt concentration in the brine is calculated by the CST-LB model. In the case of salt precipitation, the CNT is adopted to calculate nucleation kinetics on the solid surface and the growth of precipitates is treated as heterogeneous chemical reactions. The overall numerical implementation for coupling the above models will be illustrated at the end of this section.

2.1. Pseudopotential model for gas–brine multiphase flow and brine evaporation

The LB equation of fluid flow for the σ th component ($\sigma = g$ for gas, $\sigma = b$ for brine) with the multiple-relaxation-time (MRT) collision operator can be written as (Guo and Zheng, 2008)

$$\begin{aligned} \mathbf{f}^\sigma(\mathbf{x}, t) &= \mathbf{f}^\sigma(\mathbf{x}, t) - \mathbf{M}^{-1} \mathbf{\Lambda}^\sigma [\mathbf{m}^\sigma(\mathbf{x}, t) - \mathbf{m}^{\sigma, \text{eq}}(\mathbf{x}, t)] + \Delta t \cdot \mathbf{M}^{-1} \left(\mathbf{I} - \frac{\mathbf{\Lambda}^\sigma}{2} \right) \mathbf{S}_F^\sigma \\ f_\alpha^\sigma(\mathbf{x} + \mathbf{e}_\alpha \Delta t, t + \Delta t) &= f_\alpha^{\sigma*}(\mathbf{x}, t) \end{aligned} \quad (1)$$

where $\mathbf{f}^\sigma = [f_0^\sigma, \dots, f_\alpha^\sigma, \dots, f_{q-1}^\sigma]^T$ containing f_α^σ is the density distribution function of the σ th component at the direction α , position \mathbf{x} , and time t . \mathbf{M} is the transformation matrix with $\mathbf{m}^\sigma = \mathbf{M}\mathbf{f}^\sigma$ and $\mathbf{\Lambda}^\sigma$ is the diagonal relaxation matrix. $\mathbf{m}^{\sigma, \text{eq}}$ is the equilibrium density distribution function moment and \mathbf{S}_F^σ is the force term. Δx and Δt are lattice space and time

step, respectively, which are set as unity in the lattice unit. In the present work, the D3Q19 lattice model is used, which has been demonstrated in our previous work to effectively solve the governing equations for multiphase flow (Fei et al., 2019; Wang et al., 2022). For D3Q19 model, the discrete velocities \mathbf{e}_α and the transformation matrix \mathbf{M} are written as (Rahimi et al., 2019)

The equilibrium moment $\mathbf{m}^{\sigma, \text{eq}}$ and force term \mathbf{S}_F^σ are given by

$$\begin{aligned} \mathbf{m}^{\sigma, \text{eq}} &= \left[\rho^\sigma, -11\rho^\sigma + 19\rho^\sigma(u_x^2 + u_y^2 + u_z^2), 3\rho^\sigma \right. \\ &\quad \left. -11\rho^\sigma(u_x^2 + u_y^2 + u_z^2)/2, \right. \\ &\quad \left. \rho^\sigma u_x, -2\rho^\sigma u_x/3, \rho^\sigma u_y, -2\rho^\sigma u_y/3, \rho^\sigma u_z, -2\rho^\sigma u_z/3, \right. \\ &\quad \left. \rho^\sigma(2u_x^2 - u_y^2 - u_z^2), -\rho^\sigma(2u_x^2 - u_y^2 - u_z^2) \right. \\ &\quad \left. / 2, \rho^\sigma(u_y^2 - u_z^2), \rho^\sigma(u_z^2 - u_y^2) / 2, \right. \\ &\quad \left. \rho^\sigma u_x u_y, \rho^\sigma u_y u_z, \rho^\sigma u_z u_x, 0, 0, 0 \right]^T \end{aligned} \quad (4)$$

$$\begin{aligned} \mathbf{S}_F^\sigma &= \left[0, 38(u_x F_x^\sigma + u_y F_y^\sigma + u_z F_z^\sigma), -11(u_x F_x^\sigma + u_y F_y^\sigma + u_z F_z^\sigma), \right. \\ &\quad \left. F_x^\sigma, -2F_x^\sigma/3, F_y^\sigma, -2F_y^\sigma/3, F_z^\sigma, -2F_z^\sigma \right. \\ &\quad \left. / 3, 2(2u_x F_x^\sigma - u_y F_y^\sigma - u_z F_z^\sigma), \right. \\ &\quad \left. -2c F_x^\sigma + u_y F_y^\sigma + u_z F_z^\sigma, 2(u_y F_y^\sigma - u_z F_z^\sigma), -u_y F_y^\sigma + u_z F_z^\sigma, \right. \\ &\quad \left. u_y F_x^\sigma + u_x F_y^\sigma, u_z F_y^\sigma + u_y F_z^\sigma, u_x F_z^\sigma + u_z F_x^\sigma, 0, 0, 0 \right]^T \end{aligned} \quad (5)$$

where ρ^σ is the fluid density, $\mathbf{u} = [u_x, u_y, u_z]$ is the fluid velocity and $\mathbf{F}^\sigma = [F_x^\sigma, F_y^\sigma, F_z^\sigma]$ is the force applied to the fluid. The diagonal relaxation matrix $\mathbf{\Lambda}^\sigma$ contains parameters related to the fluid viscosity and diffusivity as

$$\Lambda^\sigma = \text{diag} \left(0, \omega_e^\sigma, \omega_\varepsilon^\sigma, \omega_j^\sigma, \omega_q^\sigma, \omega_j^\sigma, \omega_q^\sigma, \omega_j^\sigma, \omega_q^\sigma \right) \quad (6)$$

where ω_e^σ and ω_v^σ are related to the bulk viscosity ξ^σ and kinematic viscosity v^σ as

$$\begin{aligned} \xi^\sigma &= \frac{2}{9} \left(\frac{1}{\omega_e^\sigma} - \frac{1}{2} \right) \frac{\Delta x^2}{\Delta t} \\ v^\sigma &= \frac{1}{3} \left(\frac{1}{\omega_v^\sigma} - \frac{1}{2} \right) \frac{\Delta x^2}{\Delta t} \end{aligned} \quad (7)$$

ω_e^σ , ω_q^σ , ω_π^σ and ω_m^σ are adjustable parameters to improve the numerical stability and ω_j^σ is the parameter to set the diffusivity of the σ th component in mass transfer, which will be discussed in detail below. The density and velocity of each component are determined by

$$\rho^\sigma = \sum f_a^\sigma, \rho^\sigma \mathbf{u}^\sigma = \sum f_a^\sigma \mathbf{e}_a + \frac{\Delta t}{2} \mathbf{F}^\sigma \quad (8)$$

and the total density and mixture velocity are (Chai and Zhao, 2012)

$$\rho = \sum \rho^\sigma, \mathbf{u} = \sum \rho^\sigma \mathbf{u}^\sigma / \sum \rho^\sigma \quad (9)$$

For the pseudopotential LB model, both the intracomponent force $\mathbf{F}_{\sigma\sigma}$ and the intercomponent force $\mathbf{F}_{\sigma\bar{\sigma}}$ are introduced in the present work to realize multicomponent multiphase phase flow involving the fluid EOS. The intracomponent force is adopted to introduce the EOS by (Li et al., 2016)

$$\mathbf{F}_{\sigma\sigma} = -G_{\sigma\sigma}\psi^\sigma(\mathbf{x}) \sum_a w(|\mathbf{e}_a|^2) \psi^\sigma(\mathbf{x} + \mathbf{e}_a) \mathbf{e}_a \quad (10)$$

where the pseudopotential ψ^σ is determined by the fluid EOS as

$$\psi^\sigma(\rho^\sigma) = \sqrt{\frac{2}{G_{\sigma\sigma}}} (p_{\text{EOS}}^\sigma - c_s^2 \rho^\sigma) \quad (11)$$

$c_s = \Delta x / \sqrt{3} \Delta t$, $G_{\sigma\sigma} = \text{sign}(p_{\text{EOS}}^\sigma - c_s^2 \rho^\sigma)$. w is the weight factor, which is set as $w(1) = 1/6$, $w(2) = 1/12$ in D3Q19 framework. Various EOSs can be incorporated into the pseudopotential model (Yuan and Schaefer, 2006) and the present work chooses the Carnahan–Starling scheme as

$$p_{\text{EOS}}^\sigma = \rho^\sigma RT \frac{1 + b\rho^\sigma / 4 + (b\rho^\sigma / 4)^2 - (b\rho^\sigma / 4)^3}{(1 - b\rho^\sigma / 4)^3} - a\rho^\sigma \quad (12)$$

where a and b are coefficients of the EOS which can be used to adjust the density ratio of the saturated vapour and liquid. The intercomponent force to simulate the multicomponent multiphase flow of components σ and $\bar{\sigma}$ is computed by (Li et al., 2016)

$$\mathbf{F}_{\sigma\bar{\sigma}} = -G_{\sigma\bar{\sigma}}\varphi^\sigma(\mathbf{x}) \sum_a w(|\mathbf{e}_a|^2) \varphi^{\bar{\sigma}}(\mathbf{x} + \mathbf{e}_a) \mathbf{e}_a \quad (13)$$

with the pseudopotential φ^σ being

$$\varphi^\sigma(\rho^\sigma) = 1 - \exp(-\rho^\sigma / \rho_0^\sigma) \quad (14)$$

$G_{\sigma\bar{\sigma}}$ determines the surface tension at the interface and ρ_0^σ is usually chosen according to the density of the fluid component σ . The total force applied to σ can be calculated by

$$\mathbf{F}^\sigma = \mathbf{F}_{\sigma\sigma} + \mathbf{F}_{\sigma\bar{\sigma}} \quad (15)$$

In the present work, the gas phase is regarded as an ideal gas, and the intracomponent force is only applied on brine fluid with $\mathbf{F}_{gg} = 0$. The boundary condition treatment at the solid surface adopts the local-average virtual density scheme proposed in our previous work (Yang et al., 2022) to adjust the contact angle. With the Chapman–Enskog analysis, the above LB equations recover the Navier–Stokes equations as

(Li et al., 2013)

$$\begin{aligned} \frac{\partial \rho}{\partial t} + \nabla \cdot (\rho \mathbf{u}) &= 0 \\ \frac{\partial(\rho \mathbf{u})}{\partial t} + \nabla \cdot (\rho \mathbf{u} \mathbf{u}) &= -\nabla p + \nabla \cdot (\rho v(\nabla \mathbf{u} + (\nabla \mathbf{u})^T)) + \nabla \left(\rho \left(\xi - \frac{2}{3} v \right) (\nabla \cdot \mathbf{u}) \right) \end{aligned} \quad (16)$$

with the total pressure

$$p = \sum_\sigma \left(p_{\text{EOS}}^\sigma + \frac{1}{2} G_{\sigma\bar{\sigma}} \varphi_\sigma \varphi_{\bar{\sigma}} \right) \quad (17)$$

In addition to the Navier–Stokes equations, the advection–diffusion equation describing the mass transfer of fluid component σ can also be derived from Chapman–Enskog analysis as (Guo et al., 2022)

$$\frac{\partial Y^\sigma}{\partial t} + \nabla \cdot (Y^\sigma \mathbf{u}) = -\nabla(\rho D^\sigma \nabla Y^\sigma + D^\sigma \nabla p) \quad (18)$$

where $Y^\sigma = \rho^\sigma / \rho$ is the mass fraction of the fluid component σ . The right side of the equation represents diffusion driven by the mass fraction gradient and pressure gradient, respectively. In the present work, we focus on the diffusion driven by mass fraction gradient. According to Guo et al.’s analysis (Guo et al., 2022), the diffusion coefficient D^σ has an explicit expression as

$$\begin{aligned} D^\sigma &= \left(\frac{1}{\omega_j^\sigma} - \frac{\Delta t}{2} \right) \left(\frac{P_{\sigma\bar{\sigma}} Q_\sigma - P_{\sigma\sigma} Q_{\bar{\sigma}}}{Q_\sigma Y^\sigma + Q_{\bar{\sigma}}(1 - Y^\sigma)} \right) \\ P_{\sigma\bar{\sigma}} &= c_s^2 Y^\sigma + Y^\sigma G_{\sigma\bar{\sigma}} \varphi^{\bar{\sigma}} (\partial \varphi^{\bar{\sigma}} / \partial \rho^{\bar{\sigma}}) + Y^\sigma G_{\sigma\bar{\sigma}} \varphi^\sigma (\partial \varphi^\sigma / \partial \rho^\sigma) \\ P_{\sigma\sigma} &= c_s^2 (Y^\sigma - 1) + (Y^\sigma - 1) G_{\sigma\sigma} \psi^\sigma (\partial \psi^\sigma / \partial \rho^\sigma) + (Y^\sigma - 1) G_{\sigma\bar{\sigma}} \varphi^{\bar{\sigma}} (\partial \varphi^\sigma / \partial \rho^\sigma) \\ Q_\sigma &= c_s^2 + G_{\sigma\sigma} \psi^\sigma (\partial \psi^\sigma / \partial \rho^\sigma) + G_{\sigma\bar{\sigma}} \varphi^{\bar{\sigma}} (\partial \varphi^\sigma / \partial \rho^\sigma) \end{aligned} \quad (19)$$

It is observed that the diffusion coefficient can be adjusted by the relaxation parameter ω_j^σ , but the explicit correspondence between D^σ and ω_j^σ is too complicated. How to set a reasonable ω_j^σ conveniently to achieve the target diffusion coefficient D^σ in the simulation is the key issue. During brine evaporation, the mass transfer of brine vapour in the gas phase is of most interest. Appropriately, in the typical Stefan problem (Stephen, 2000), the diffusion coefficient of brine vapour in the gas phase determines the evaporation rate. Therefore, it is possible to invert the diffusion coefficient by modelling the Stefan problem. This post-derivative approach provides a more straightforward solution to obtain the diffusion coefficient and its operation will be introduced in Section 3.

2.2. CST-LB model for salt mass transfer in brine

The mass transfer of salt species in brine is a typical advection–diffusion process. Although the CST-LB model was initially designed to calculate the interfacial mass transfer between two solvent phases, its ability to calculate solute transport in only one solvent phase was also proved in our previous work by setting an extremely large or small Henry coefficient (Yang et al., 2021). Therefore, the CST-LB model is adopted here for salt mass transfer. The D3Q7 MRT CST-LB model, which is discretised on the first seven directions in Eq. (2) without significant accuracy loss (Chen et al., 2020), is given by

$$\begin{aligned} \mathbf{g}^*(\mathbf{x}, t) &= \mathbf{g}(\mathbf{x}, t) - \mathbf{N}^{-1} \left(\Lambda^s(\mathbf{n}(\mathbf{x}, t) - \mathbf{n}^{\text{eq}}(\mathbf{x}, t)) + \Delta t \left(\mathbf{I} - \frac{\Lambda^s}{2} \right) \mathbf{S}_{\text{CST}} \right) \\ g_a(\mathbf{x} + \mathbf{e}_a \Delta t, t + \Delta t) &= g_a^*(\mathbf{x}, t) \end{aligned} \quad (20)$$

where $\mathbf{g}^\sigma = [g_0^\sigma, \dots, g_a^\sigma, \dots, g_{q-1}^\sigma]^T$ is the concentration distribution function ($q = 7$). \mathbf{N} is the transformation matrix with $\mathbf{n} = \mathbf{N} \mathbf{g}$. Λ^s represents the diagonal relaxation matrix for salt mass transfer and \mathbf{S}_{CST} is the CST

additional term to realize the concentration step at the gas–brine interface. For D3Q7 model, the transformation matrix is given by

$$\mathbf{N} = \begin{bmatrix} 1 & 1 & 1 & 1 & 1 & 1 & 1 \\ 0 & 1 & -1 & 0 & 0 & 0 & 0 \\ 0 & 0 & 0 & 1 & -1 & 0 & 0 \\ 0 & 0 & 0 & 0 & 0 & 1 & -1 \\ 6 & -1 & -1 & -1 & -1 & -1 & -1 \\ 0 & 2 & 2 & -1 & -1 & -1 & -1 \\ 0 & 0 & 0 & 1 & 1 & -1 & -1 \end{bmatrix} \quad (21)$$

The equilibrium concentration distribution function and the equilibrium moment \mathbf{n}^{eq} are calculated based on the salt concentration C_s as

$$g_a^{\text{eq}} = C_s \cdot (w_a + 0.5 \mathbf{e}_a \cdot \mathbf{u}) \quad (22)$$

$$w_a = \begin{cases} 1/4 & \alpha = 0 \\ 1/8 & \alpha = 1 \sim 6 \end{cases}$$

$$\mathbf{n}^{\text{eq}} = \left[C_s, C_s u_x, C_s u_y, C_s u_z, \frac{3}{4} C_s, 0, 0 \right]^T \quad (23)$$

The diagonal relaxation matrix $\Lambda^s = \text{diag}(\omega_0, \omega_D, \omega_D, \omega_D, \omega_4, \omega_5, \omega_6)$ contains the parameter ω_D related to the salt diffusion coefficient D_s as

$$D_s = \frac{1}{4} \left(\frac{1}{\omega_D} - \frac{1}{2} \right) \frac{\Delta x^2}{\Delta t} \quad (24)$$

and the other parameters are set as unity (Chen et al., 2020). The CST additional term can be written as

$$\mathbf{S}_{\text{CST}} = \frac{1}{4} C_s \frac{H - 1}{H x_b + (1 - x_b)} \left[0, \frac{\partial x_b}{\partial x}, \frac{\partial x_b}{\partial y}, \frac{\partial x_b}{\partial z}, 0, 0, 0 \right]^T \quad (25)$$

where H is the Henry coefficient to describe the concentration distribution at the gas–brine interface as $C_s^b = H C_s^g$. C_s^b and C_s^g are salt concentrations in the brine and the gas phase, respectively. In the present work, H is set by a very large number as $H = 1000$ to simulate the presence of salt only in the brine phase with $C_s^g \approx 0$. x_b is the phase fraction of brine which is calculated by the pseudopotential φ as recommended in our previous work (Yang et al., 2021)

$$x_b = \frac{\varphi^b}{\varphi^b + \varphi^g} \quad (26)$$

$x_b \approx 1$ in the brine phase while $x_b \approx 0$ in the gas. The salt concentration $C_s = x_b C_s^b + (1 - x_b) C_s^g$ is obtained by

$$C_s = \sum g_a \quad (27)$$

Using the Chapman–Enskog analysis, the above LB equation can be derived into the advection–diffusion equation with CST additional term as (Yang et al., 2021)

$$\frac{\partial C_s}{\partial t} + \nabla \cdot (C_s \mathbf{u}) = \nabla \left(D_s \nabla C_s - C_s \frac{D_s(H - 1)}{H x_b + (1 - x_b)} \nabla x_b \right) \quad (28)$$

which is equivalent to the conventional CST model (Haroun et al., 2010). It should be noted that Eq. (28) holds for the dilute solutions. For the sake of simplicity in this study, we uphold the assumption of dilute solution, despite the fact that salt concentration can escalate during the evaporation process, leading to some inaccuracies in the effective diffusivity and advection term. For improvement, the concentrated solution theory can be employed (Newman and Balsara, 2021) by adjusting the diffusivity and velocity in Eq. (28) to consider the effect of interaction between the salt ions, which may be considered in future work. Given that the conventional CST model can realize the concentration jump at the interface while ensuring the flux continuity across the interface (Graveleau et al., 2017), the mass conservation of salt during brine evaporation can also be satisfied with the CST-LB model, which will be proven in Section 3.

2.3. Salt precipitate nucleation and growth model

Two major assumptions are made in the simulation of salt precipitate nucleation: (1) The nucleation follows the classical pathway described by the classical nucleation theory; and (2) Salt is only precipitated on the solid surface with heterogeneous nucleation. The large specific surface area and small pore volume of general porous media allow for the neglect of homogeneous nucleation in the bulk of brine. Accordingly, the heterogeneous nucleation rate J_n can be calculated in the numerical model by CNT (Li et al., 2014) as

$$J_n = J_0 \exp \left(-\frac{\Delta G_n}{k_B T_n} \right) = J_0 \exp \left(-\frac{\beta (V_m / N_A)^2 \gamma^3}{k_B^3 T_n^3 (\ln \Omega)^2} \right) \quad (29)$$

where J_0 is the pre-exponential factor related to the frequency of collision, ΔG_n is the free energy barrier to form a nucleus. $k_B = 1.38 \times 10^{-23} \text{ J/K}$ is the Boltzmann constant, T_n is the temperature. β is the geometry factor based on the nucleus shape. For spherical nuclei during homogeneous nucleation, $\beta = 16\pi/3$. In the present work, although heterogeneous nucleation is concerned, the geometry factor is also set as a numerical constant $16\pi/3$ for simplicity according to the previous work (Starchenko, 2022). V_m is the molar volume of salt and $N_A = 6.02 \times 10^{23} \text{ mol}^{-1}$ is the Avogadro number. γ is the interfacial free energy. $\ln \Omega$ is the supersaturation for the salt $A_m B_n$ as

$$\ln \Omega = \ln (C_s^{m+n} / K_{sp}) \quad (30)$$

where K_{sp} is the solubility product of salt. We set $m = n = 1$ in the present work to represent typical salts, such as sodium chloride (NaCl) and calcium carbonate (CaCO₃).

Besides the nucleation rate, the nucleation probability is also a critical parameter in the numerical model since the nucleation process is stochastic. The nucleation is treated as a stochastic event with a probability distribution function of (Starchenko, 2022)

$$dP_n = x_b J_n A_s \exp(-J_n A_s t) dt \quad (31)$$

where A_s is the surface area of the solid. The use of phase fraction adjacent to the solid surface x_b is to ensure that nuclei are only formed in the brine phase neighbouring the solid nodes. At the surface of each solid node, the nucleation probability P_n is calculated by (Starchenko, 2022)

$$P_n(t + \Delta t) = P_n(t) + \frac{dP_n}{dt} \Delta t \quad (32)$$

Meanwhile, a probability threshold P_{cr} is artificially set for each solid node surface. After every N time steps (N is a numerical constant), i.e. $\text{mod}(t, N\Delta t) = 0$, P_n is compared with P_{cr} to determine whether nucleation occurs. If $P_n \geq P_{cr}$, nucleation happens on the solid node with an initial critical nucleus diameter l_0 and then the salt precipitate grows on the surface of this node, as shown in Fig. 1. If $P_n < P_{cr}$, P_n is set back to zero and Eq. (32) is repeated in the next N time steps. In the present work, P_{cr} is set to a completely random number in the interval from P_{cr}^{\min} to P_{cr}^{\max} at each solid node with the probability density function

$$\mathcal{P}(P_{cr} = x) = \frac{1}{P_{cr}^{\max} - P_{cr}^{\min}}, x \in [P_{cr}^{\min}, P_{cr}^{\max}] \quad (33)$$

where P_{cr}^{\min} denotes the minimum P_n threshold that a node requires to form a stable nucleus. A lower P_{cr}^{\min} value suggests that stable nuclei can be created at lower supersaturation levels, which implies it can be manipulated based on experimental observations by identifying the supersaturation corresponding to the first appearance of nucleation. The difference $P_{cr}^{\max} - P_{cr}^{\min}$ serves to quantify the randomness of nucleation within the pore structure. A larger discrepancy signifies a more erratic distribution of nucleation. Given that P_n never exceeds 1 according to Eqs. (31) and (32), P_{cr}^{\max} may be assigned a value greater than 1 to mimic scenarios in experiments where stable nuclei do not form at certain

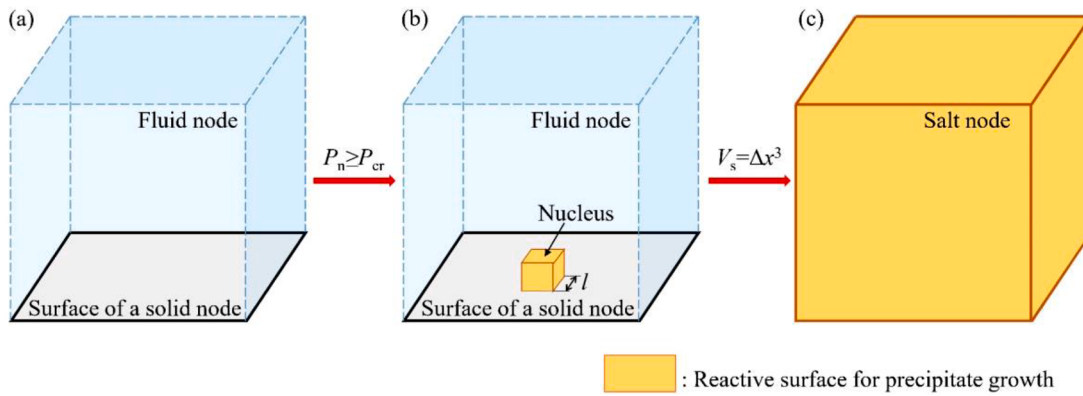


Fig. 1. Schematic diagram of numerical implementation of salt precipitate nucleation and growth. (a) A fluid node at the solid surface. (b) Nucleation on the solid surface. (c) The fluid node is transformed into a salt node with nucleus growth.

locations. There are also alternative methods of designating random numbers through different probability density functions \mathcal{P} , like the normal distribution (Fazeli et al., 2020) to more accurately replicate the actual physical conditions, which will not be further discussed in the present work.

For a better adaptation of the LB grid, the shape of nucleus is set to a cube as shown in Fig. 1(b). This treatment has been successfully employed in the previous work (Masoudi et al., 2021) to describe the nucleation process. In the numerical simulation, there are three sorts of nodes indicated, the solid node, the fluid node, and the salt node. Growth of the salt precipitates only occurs on the surface of salt nucleus and salt nodes, marked by yellow in Fig. 1. The growth of the nucleation cube eventually makes the fluid node filled with salt, becoming a salt node, as shown in Fig. 1(c). In general, the growth of salt precipitates can be described as a heterogeneous chemical reaction:



where aq denotes the salt ion in brine and s denotes the salt precipitate. Considering salt precipitate only grows in the brine phase, the reaction rate \dot{r} is given by (Starchenko, 2022)

$$\dot{r} = x_b \chi A_s k (\Omega - 1) = x_b \chi A_s k \left(\frac{C_s^2}{K_{sp}} - 1 \right) \quad (35)$$

where k is the kinetic coefficient, and χ is the surface coverage parameter indicating the reactive surface area. For a non-reactive solid node with a growing nucleus in Fig. 1(b), χ is estimated by the nucleus superficial area as

$$\chi = 5l^2 / \Delta x^2 = 5V_s^{2/3} / \Delta x^2 \quad (36)$$

where V_s is the salt volume in the adjacent fluid node. For a salt node as shown in Fig. 1(c), the whole surface is reactive for salt precipitate growth and thus $\chi = 1$. With this treatment, the rate of growth for precipitates is faster on the surfaces of previously formed precipitates. Therefore, it can effectively approximate the process known as preferential nucleation, where the new nucleation events are more likely to happen on the freshly formed precipitates due to the interfacial free energy preferences (Nooraeipour et al., 2021b). The salt volume in a fluid node is calculated by

$$V_s(t + \Delta t) = V_s(t) + \dot{r}V_m \Delta t \quad (37)$$

When V_s grows to the grid volume Δx^3 , the fluid node is converted to the salt node.

On the solid or salt node surface in the brine side, the salt mass flux should follow the reaction flux as

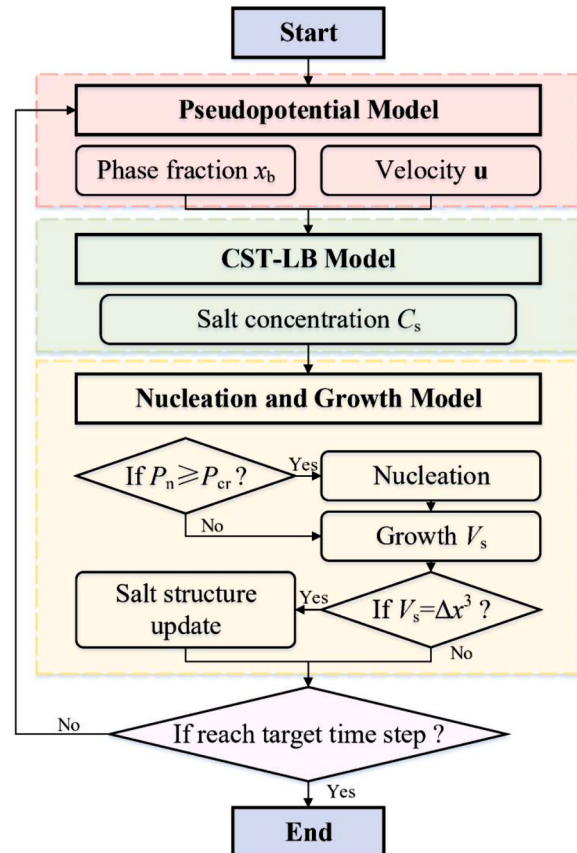


Fig. 2. Schematic diagram of the overall numerical implementation.

$$-D_s \nabla C_s + C \frac{D_s(H-1)}{Hx_b + (1-x_b)} \nabla x_b = -\dot{r}(\mathbf{x} + 0.5\mathbf{e}_a \Delta t) \mathbf{n} \quad (38)$$

where \mathbf{n} is the surface normal vector of the solid or salt node adjacent to the fluid nodes (Yang et al., 2022). Based on Eq. (38), boundary treatment in the CST-LB model is given by

$$\mathbf{e}_a g_a^*(\mathbf{x}, t) = -\dot{r}(\mathbf{x} + 0.5\mathbf{e}_a \Delta t) \mathbf{n} - \mathbf{e}_{\bar{a}} g_{\bar{a}}^*(\mathbf{x} + \mathbf{e}_a \Delta t, t) \quad (39)$$

to calculate the unknown post-collision concentration distribution function g_a^* (a and \bar{a} are in the opposite directions). More details of salt concentration boundary treatment can be found in our previous work (Yang et al., 2021).

2.4. Overall numerical implementation

The overall numerical implementation to simulate salt precipitation during brine evaporation is illustrated in Fig. 2. The pseudopotential model Eq. (1) is firstly adopted to simulate gas–brine multiphase flow and brine evaporation, providing the phase fraction x_b by Eq. (26). The phase fraction and velocity are input into the CST-LB model Eq. (20) to calculate the salt concentration in brine involving salt growth reaction by Eq. (39). Given the salt concentration, nucleation probability of salt precipitates within N time steps is computed by Eqs. (29), (31) and (32). When the total time step reaches an integer multiple of $N (\bmod(t, N\Delta t) = 0)$, P_n is compared with P_{cr} to determine whether a nucleation event occurs. Salt volume in the fluid node is computed by Eq. (37) and salt structure evolution is conducted by converting the fluid node to the salt node once V_s reaches Δx^3 . The updated salt structure is imported in the next time step to continue the salt precipitation simulation.

The numerical procedures described in this work are developed in-house with C++ and parallel programming based on message passing interface (MPI) is conducted to improve the computational efficiency. Validations of the pseudopotential model and CST-LB model can be found in our previous work (Wang et al., 2022; Yang et al., 2022, 2021), including comparisons with analytical solutions and existing numerical or experimental results to demonstrate the reliability of our numerical model.

3. Numerical application

Following the construction of the numerical models, a series of benchmark cases are performed in this section to verify the numerical performance for the simulation of salt precipitation during brine evaporation. First, the Stefan problem is simulated in order to demonstrate how to determine the gas-phase diffusion coefficient of brine vapour in the pseudopotential model. The evolution of salt concentration during brine evaporation is also calculated to verify the capacity of CST-LB model in the simulation of salt mass transfer. The simulation of salt precipitation during the evaporation of a brine droplet is then performed with different nucleation growth kinetics. Finally, we simulate the salt precipitation process during gas injection within a microfluidic chip as an application case conducted in porous media.

3.1. Brine evaporation in the Stefan problem

As mentioned before, setting the diffusion coefficient of brine vapour in the gas phase D^b explicitly is almost impossible due to its complexity as shown in Eq. (19). We thus use the Stefan problem to clarify the correspondence between the numerical parameter ω_j^g and the diffusion coefficient implicitly. The Stefan problem is illustrated in Fig. 3. The brine locates in a cylinder with a gas section at the left outlet. The length of the gas phase is L . In the gas-phase side, the brine vapour and gas are in equilibrium on the gas–brine interface, with a mass fraction Y_{eq}^b according to the saturated vapour pressure of brine. At the outlet, the mass fraction of brine vapour Y_∞^b is lower than Y_{eq}^b , bringing a driving force for mass transfer, and the brine vapour will diffuse from the gas–brine interface to the outlet of the cylinder. Mass transfer to the outlet causes the brine to evaporate continuously, leading to an increase in the gas section length L . According to Fick's law described by Eq. (18), the time-varying gas section length has the analytical solution as (Stephen, 2000)

Table 1

The value of parameter ω_j^b set in the Stefan problem with density ratio of $O(10)$, and the corresponding diffusion coefficient D^b obtained by Eq. (41).

ω_j^b	$D^b (\times 10^{-6} \text{m}^2/\text{s})$
0.667	0.46
0.400	0.87
0.182	2.05
0.118	3.09
0.095	3.75
0.049	7.15
0.020	14.05
0.010	22.08
0.000	40.94

$$\frac{dL^2}{dt} = \frac{2\rho|_g D^b \ln\left(\frac{1 - Y_\infty^b}{1 - Y_{eq}^b}\right)}{\rho|_b} \quad (40)$$

where $\rho|_g$ and $\rho|_b$ are the total fluid density in the gas phase and brine phase, respectively. By capturing the increase rate of L^2 , the diffusion coefficient D^b can be obtained by

$$D^b = \frac{dL^2}{dt} \frac{\rho|_b}{2\rho|_g} \Big/ \ln\left(\frac{1 - Y_\infty^b}{1 - Y_{eq}^b}\right) \quad (41)$$

The size of the computational domain is $6\text{mm} \times 0.38\text{mm}$ and the grid resolution is set as $\Delta x = 10\mu\text{m}$ according to mesh convergence analyses involving grid resolution $\Delta x = 5, 10, 20\mu\text{m}$. The initial length of the gas phase is $L_0 = 1\text{mm}$. The two-dimensional Stefan problem is investigated. For the pseudopotential model, the intercomponent force coefficients are $G_{bg} = G_{gb} = 1.3$ in lattice unit. The intracomponent force is only adopted on the brine component with the EOS parameters as $a = 0.09926$, $b = 0.18727$, $R = 0.2$, $T = 0.85$ in lattice unit for Eq. (12). These settings lead to the densities of gas and brine component in equilibrium as $\rho^b|_b = 6.20$, $\rho^g|_b = 0.04$ in brine phase and $\rho^b|_g = 0.14$, $\rho^g|_g = 0.59$ in gas phase respectively. (The superscript σ represents the fluid component and the subscript $|_\sigma$ represents the phase. The phase information of each node is identified by the phase fraction x_b . $x_b \geq 0.5$ indicates the brine phase and $x_b < 0.5$ indicates the gas phase.) As a result, the total densities in the gas and brine phase are $\rho|_b = 6.24$, $\rho|_g = 0.73$ in lattice unit, which is converted to $\rho|_b = 1000\text{kg/m}^3$, $\rho|_g = 117\text{kg/m}^3$ in physical unit with a density ratio of $O(10)$. The equilibrium brine mass fraction in the gas phase can be obtained by $Y_{eq}^b = \rho^b|_g / \rho|_g = 0.19$. The kinematic viscosity is set as $\nu^b = \nu^g = 1.0 \times 10^{-6} \text{m}^2/\text{s}$ and the contact angle is set as $\theta \approx 90^\circ$. The top, bottom and right boundaries of the computational domain are all non-slip solid walls and the pressure boundary is set at the left outlet with $\rho^b|_g = 0.01$, $\rho^g|_g = 0.72$ in lattice unit, resulting in the brine mass fraction at the outlet $Y_\infty^b = 0.014$.

Based on Eq. (19), ω_j^g is the key parameter for adjusting the diffusion coefficient. Therefore, different ω_j^b listed in Table 1 are adopted in the simulation to obtain different D^b . Fig. 4(a) and (b) shows the numerical results of gas–brine distribution and Y^b profile along the vertical axis with $\omega_j^b = 0.095$. As the brine evaporates, the length of gas phase continues to elongate as shown in Fig. 4(a) due to the continuous diffusion of brine vapour to the outside. In the Stefan problem, the brine mass fraction distribution in the gas phase along x -axis can be written as

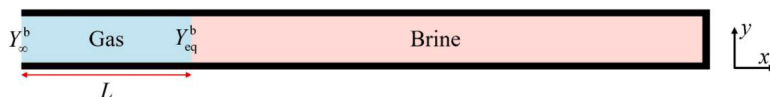


Fig. 3. Computational domain of Stefan problem.

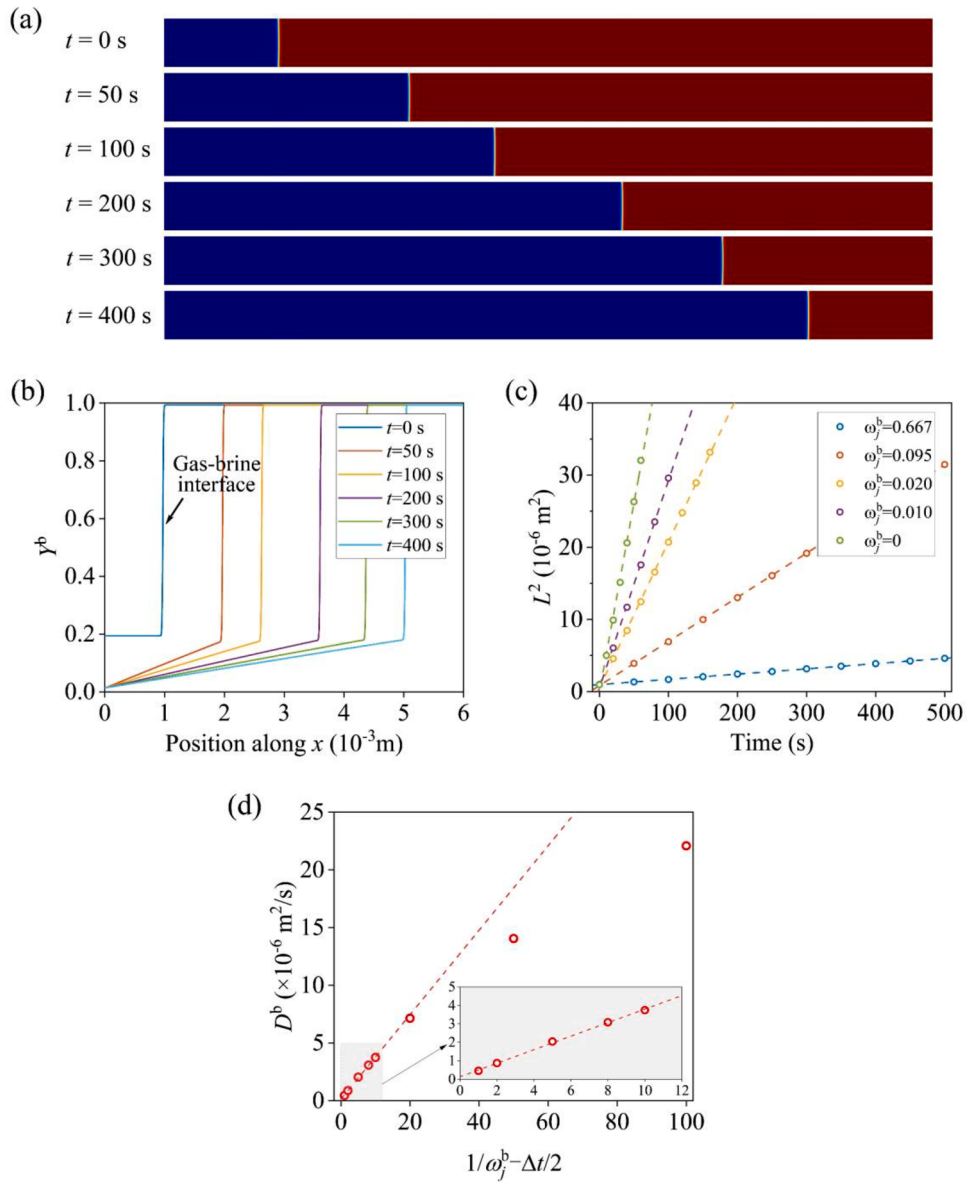


Fig. 4. Numerical results of Stefan problem (a) Phase distribution evolution with $\omega_j^b = 0.095$. The red colour represents the brine phase and the blue colour is the gas phase. (b) Brine mass fraction along x -axis at different moment with $\omega_j^b = 0.095$. (c) $L^2 - t$ curves. (d) The relationship between D^b and $1/\omega_j^b - \Delta t/2$. The red dotted line is the linear fitting curve of the data with $\omega_j^b > 0.1$.

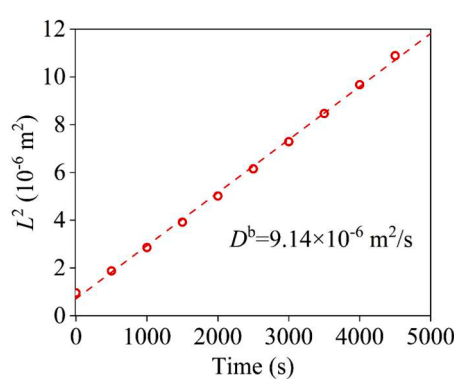


Fig. 5. $L^2 - t$ curve of Stefan problem with gas–brine density ratio at $O(10^2)$ ($\omega_j^b = 0$).

$$Y^b(x) = 1 - \left(1 - Y_{\text{eq}}^b\right) \left(1 + \frac{Y_{\text{eq}}^b - Y_{\infty}^b}{1 - Y_{\text{eq}}^b}\right)^{1-\frac{x}{L}} \quad (42)$$

When $Y_{\text{eq}}^b - Y_{\infty}^b$ is not very large, Eq. (42) can be approximated as

$$Y^b(x) = Y_{\text{eq}}^b - \left(Y_{\text{eq}}^b - Y_{\infty}^b\right) \left(1 - \frac{x}{L}\right) \quad (43)$$

Therefore, the Y^b curve exhibits an approximately linear trend at each moment in Fig. 4(b). At the gas–brine interface in the gas phase side, $Y^b = Y_{\text{eq}}^b$ constantly, indicating that the saturation vapour pressure of brine is specified by a certain set of pseudopotential model parameters. Since Y_{eq}^b and Y_{∞}^b are constant, with the increase in the length of the gas phase, the gradient of Y^b decreases as shown in Fig. 4(b), resulting in the reduced driving force for brine vapour mass transfer. To obtain the diffusion coefficient of brine vapour, the variation of L^2 with time is plotted in Fig. 4(c). L^2 and time show an excellent linear relationship with different ω_j^b , and the linear fitting result is also plotted in Fig. 4(c).

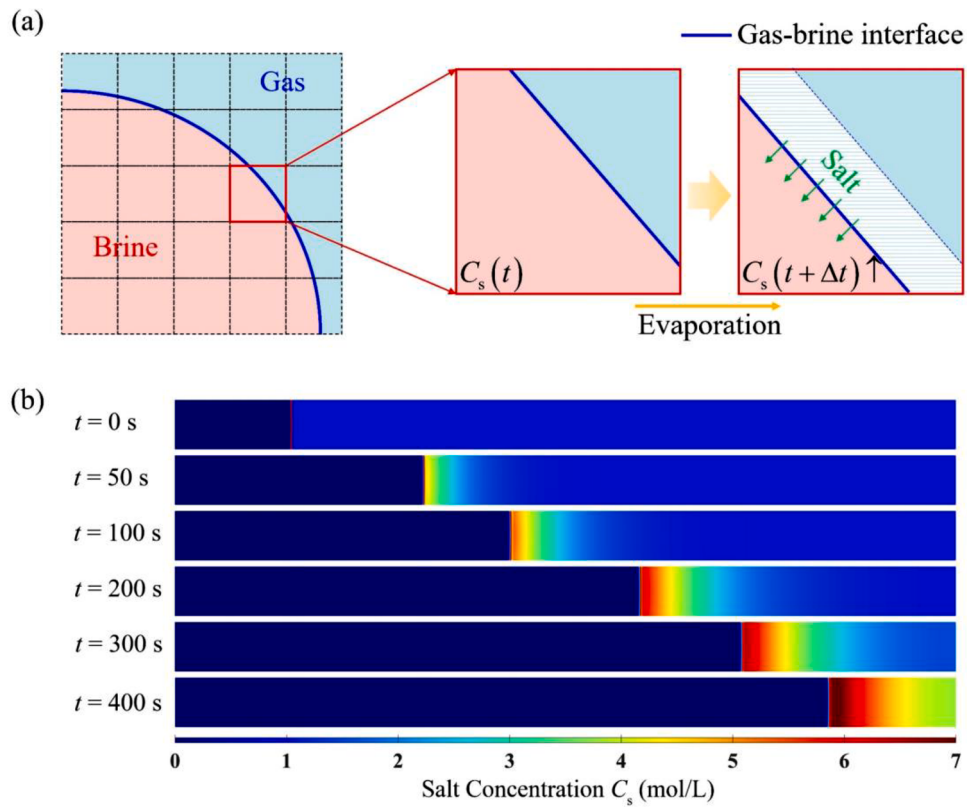


Fig. 6. (a) Schematic diagram to describe how the CST model achieves salt mass conservation in a node at the interface. The salt in the evaporated brine (dash area at $t + \Delta t$) will be counted into the remaining brine during evaporation. (b) Numerical results of salt concentration evolution during Stefan problem.

By taking the slope of $L^2 - t$ fitting line into Eq. (41), the diffusion coefficient of brine vapour D^b can be obtained, which is listed in Table 1. The value of D^b has a wide adjustable range of $O(10^{-7}) \sim O(10^{-5})\text{m}^2/\text{s}$, which is appropriate for most situations in nature. The relationship between ω_j^b and D^b is plotted in Fig. 4(d) to clarify the basis for setting the target diffusion coefficient. When $1/\omega_j^b - \Delta t/2$ is not large (less than $O(10)$, corresponding to $\omega_j^b > 0.1$), D^b shows a linear relationship with $1/\omega_j^b - \Delta t/2$, which is consistent with Eq. (19). However, as ω_j^b continues to decrease ($1/\omega_j^b - \Delta t/2 > O(10)$), the resulting D^b deviates from this linear relationship. The deviation indicates when ω_j^b is small, it is inaccurate to describe the correspondence between D^b and ω_j^b by virtue of the linear relationship in Eq. (19). To find the exact value of ω_j^b for setting the target D^b , interpolation should be employed.

Motivated by the above calculation process, we propose a procedure for setting the diffusion coefficient in the pseudopotential model. Before simulation, one can conduct a series of Stefan problems with different ω_j^σ to find the correspondence between ω_j^σ and D^σ . Based on this correspondence, ω_j^σ can be adjusted by interpolation until the exported D^σ is close to the target value. It should be noticed that the correspondence between ω_j^σ and D^σ changes with the fluid densities and pseudopotentials according to Eq. (19). To corroborate this point, we calculate the Stefan problem with a different larger gas–brine density ratio. $G^{bg} = G^{bg} = 0.04$ for intercomponent force, and $T = 0.70$ for intracomponent force of brine component, leading to the fluid densities $\rho^b|_b = 7.62$, $\rho^g|_b = 0.001$, $\rho^b|_g = 0.01$, $\rho^g|_g = 0.045$ in lattice unit with the gas–brine total density ratio on $O(10^2)$. $Y_{eq}^b = 0.022$ and Y_∞^b is set as 0.002 at the outlet. Fig. 5 plots the numerical result of $L^2 - t$ curve with $\omega_j^b = 0$, which also shows a good linear relationship. With the slope of the fitting line, the diffusion coefficient is obtained as $D^b = 9.14 \times 10^{-6}\text{m}^2/\text{s}$, which is different from the result in Table 1. Therefore, when changing the numerical settings in the pseudopotential model, the Stefan problem needs

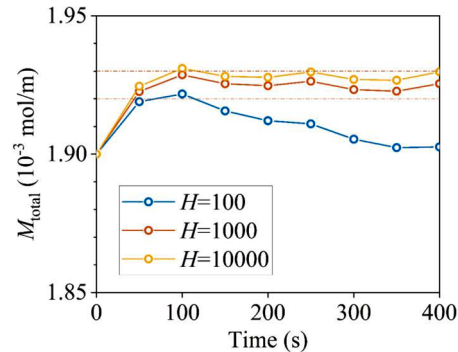


Fig. 7. The total amount of substance of salt counted at different moments.

to be re-calculated to specify the new correspondence between ω_j^σ and D^σ .

3.2. Salt mass transfer during the Stefan problem

During the salt precipitation process, the salt solute only dissolves in the brine phase. The increase in salt concentration comes from the change of brine volume. Therefore, the mass conservation of salt in brine is the crucial factor to ensure the accuracy of salt concentration. Given that the conventional CST model in the VOF framework is derived based on the conservation equation and volume average (Haroun et al., 2010), when the phase fraction of solvent in a node is changed, the solute concentration in this node will change correspondingly to meet the mass conservation, as illustrated in Fig. 6(a). If a portion of the brine evaporates in a node, the salt in this portion will be counted into the residual brine of this node. Since the CST-LB model is derived from the conventional CST model, it can also deal with the mass conservation at the

gas-brine interface. It should be noted that, in the present work, the Henry coefficient is set at an extremely high value ($H = 1000$) instead of infinity so that the salt only exists in the brine. It remains to be verified whether this setup ensures the mass conservation of salt in brine.

To verify the accuracy of the numerical settings in the CST-LB model, salt species mass transfer in brine is calculated in the Stefan problem of Section 3.1. The simulation of gas-brine multiphase flow adopts the parameters with $\rho|_b = 1000\text{kg/m}^3$, $\rho|_g = 117\text{kg/m}^3$, $D^b = 3.75 \times 10^{-6}\text{m}^2/\text{s}$. Initially, the brine contains salt with a concentration $C_s = 1\text{mol/L}$, and the diffusion coefficient of salt in brine is $D_s = 5.0 \times 10^{-9}\text{m}^2/\text{s}$. The numerical results of salt concentration evolution are shown in Fig. 6(b). The brine evaporation results in a continuous increase in salt concentration at the gas-brine interface and transport into the brine bulk by diffusion. At the gas-brine interface, the salt concentration undergoes a significant increase and eventually increases nearly tenfold at $t = 400\text{s}$.

To verify the salt mass conservation, the total amount of substance of

salt is computed at different moments by accumulating the amount of substance in each brine node as

$$M_s = \sum_{\text{brinenodes}} C_s \Delta x^2 \quad (44)$$

Fig. 7 plots M_s against time in the simulation. To assess the suitability of the numerical setup, different Henry coefficients are employed for comparison. In the case of $H = 1000$, M_s experienced a slight rise in the initial stage from $1.90 \times 10^{-3}\text{mol/m}$ to $1.92 \times 10^{-3}\text{mol/m}$. This derivation originates mainly from the initial concentration conditions not reaching equilibrium in the simulation. Subsequently, M_s fluctuates in a narrow range between $1.92 \times 10^{-3}\text{mol/m}$ and $1.93 \times 10^{-3}\text{mol/m}$ (represented by the red dot line in Fig. 7) throughout the simulation process, indicating the mass conservation is generally adequate. The accuracy of the numerical models is satisfactory with a relative error less than 2 %, which can serve for the subsequent salt precipitation simulations. When the Henry coefficient is set at a lower value 100, the

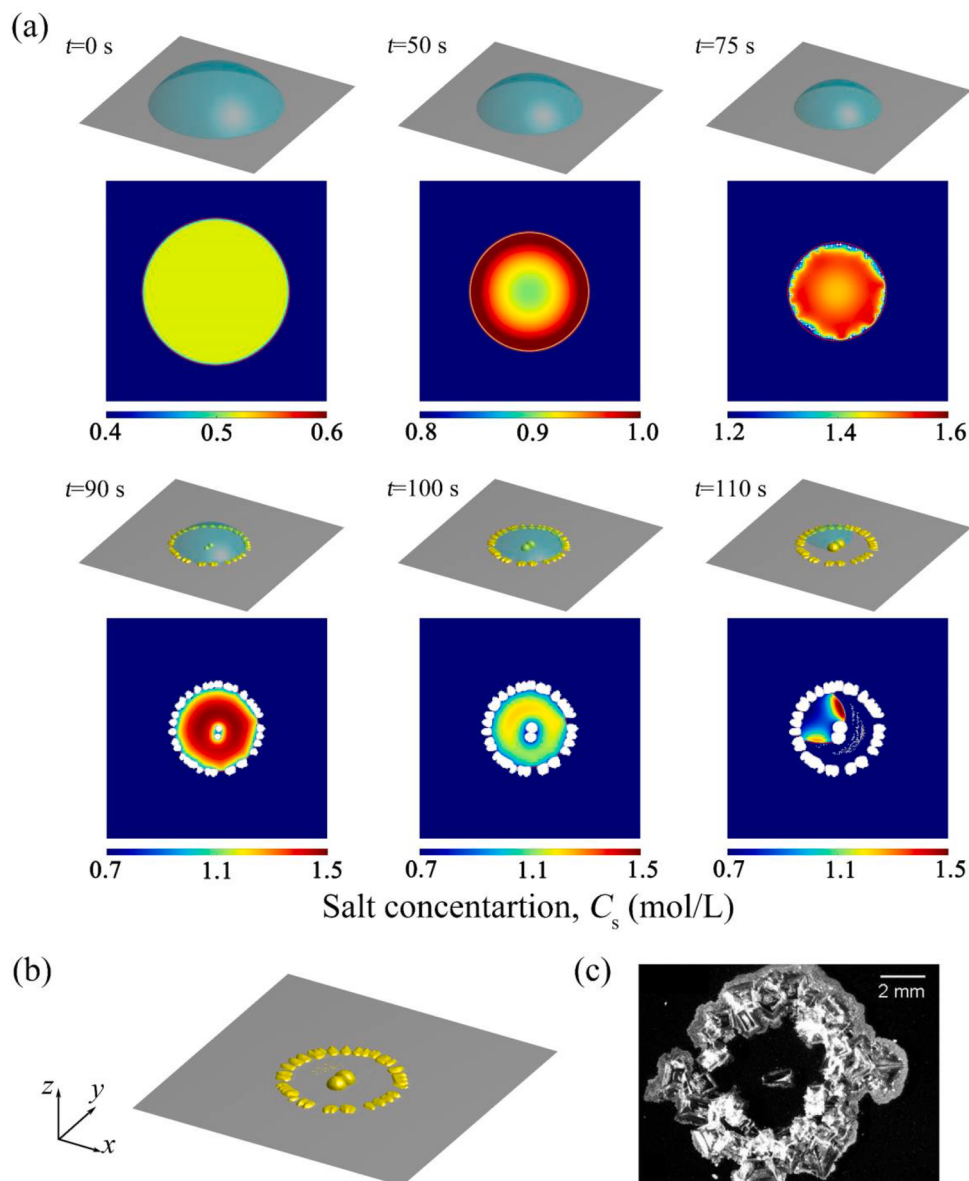


Fig. 8. (a) Numerical results of salt precipitation during brine droplet evaporation with $J_0 = 10^4$, $k = 3.81 \times 10^{-2}\text{mol}/(\text{s} \cdot \text{m}^2)$. The upper stereogram illustrates the shape of brine droplet (cyan colour) and salt precipitate distribution (yellow colour). The lower contour map exhibits the salt concentration distribution in brine at the bottom solid surface (x - y cross section) where the white colour represents salt precipitate. (b) Final salt precipitate distribution in the simulation. (c) Previous experimental observation of sodium chloride precipitation after droplet evaporation (Shahidzadeh-Bonn et al., 2008).

numerical result is different. The total amount of substance similarly undergoes a short rise in the initial stage, but then begins to gradually decline. At this point, a part of the salt enters the gas phase by the interfacial mass transfer due to the Henry coefficient not being truly infinite. Therefore, the lower Henry coefficient of 100 does not satisfy the requirement of numerical accuracy. With a higher Henry coefficient setting as $H = 10,000$, the numerical result is basically identical to the case of $H = 1000$ and M_s remains stable at around 1.93×10^{-3} mol/m, suggesting that increasing H will have little effect on the numerical performance. Based on the above comparison, it is reasonable to set H as 1000 when calculating salt mass transfer in the brine.

3.3. Salt precipitation during brine droplet evaporation

After verifying the simulation of evaporation-induced salt concentration change, salt precipitation during droplet evaporation is simulated to demonstrate the numerical performance of salt precipitate nucleation and growth model. The size of the computational domain is $2\text{mm} \times 2\text{mm} \times 2\text{mm}$ meshed by $200 \times 200 \times 200$. The computational

domain is filled with gas and a brine droplet is placed on the bottom wall. Periodic boundary conditions are employed in the x and y directions. The shape of the droplet is shown in Fig. 8(a) at $t = 0$ s, with the contact angle $\theta \approx 57^\circ$ and base circle diameter $d = 1.3\text{mm}$. The densities and kinematic viscosities of the gas and brine phases are $\rho|_b = 1000\text{kg/m}^3$, $\rho|_g = 117\text{kg/m}^3$, $\nu^b = \nu^g = 1.0 \times 10^{-6}\text{m}^2/\text{s}$. The top border of the computational domain is set as an outlet with a pressure boundary of $\rho|_{g,\infty} = 117\text{kg/m}^3$, $Y_\infty^b = 0.14$. The brine vapour transports towards the outlet due to the mass fraction gradient, leading to the further evaporation of the brine droplet. The diffusion coefficient of brine vapour and equilibrium brine mass fraction on the gas–brine interface are $D^b = 0.46 \times 10^{-6}\text{m}^2/\text{s}$, $Y_{eq}^b = 0.19$. During brine droplet evaporation, salt concentration increases, inducing salt precipitation. The solubility product and the diffusion coefficient of salt are $K_{sp} = 0.33\text{mol}^2/\text{L}^2$, $D_s = 5.0 \times 10^{-9}\text{m}^2/\text{s}$. Initially, the brine droplet is saturated with salt as $\Omega = 1$. As the salt concentration increases, salt precipitate nucleation and growth are triggered. The interfacial free energy of salt is chosen as $\gamma = 0.04\text{J/mol}$ according to the experimental data (Li et al., 2014). The initial critical nucleus diameter is set as $l_0 = 100\text{nm}$. The molar volume of salt is

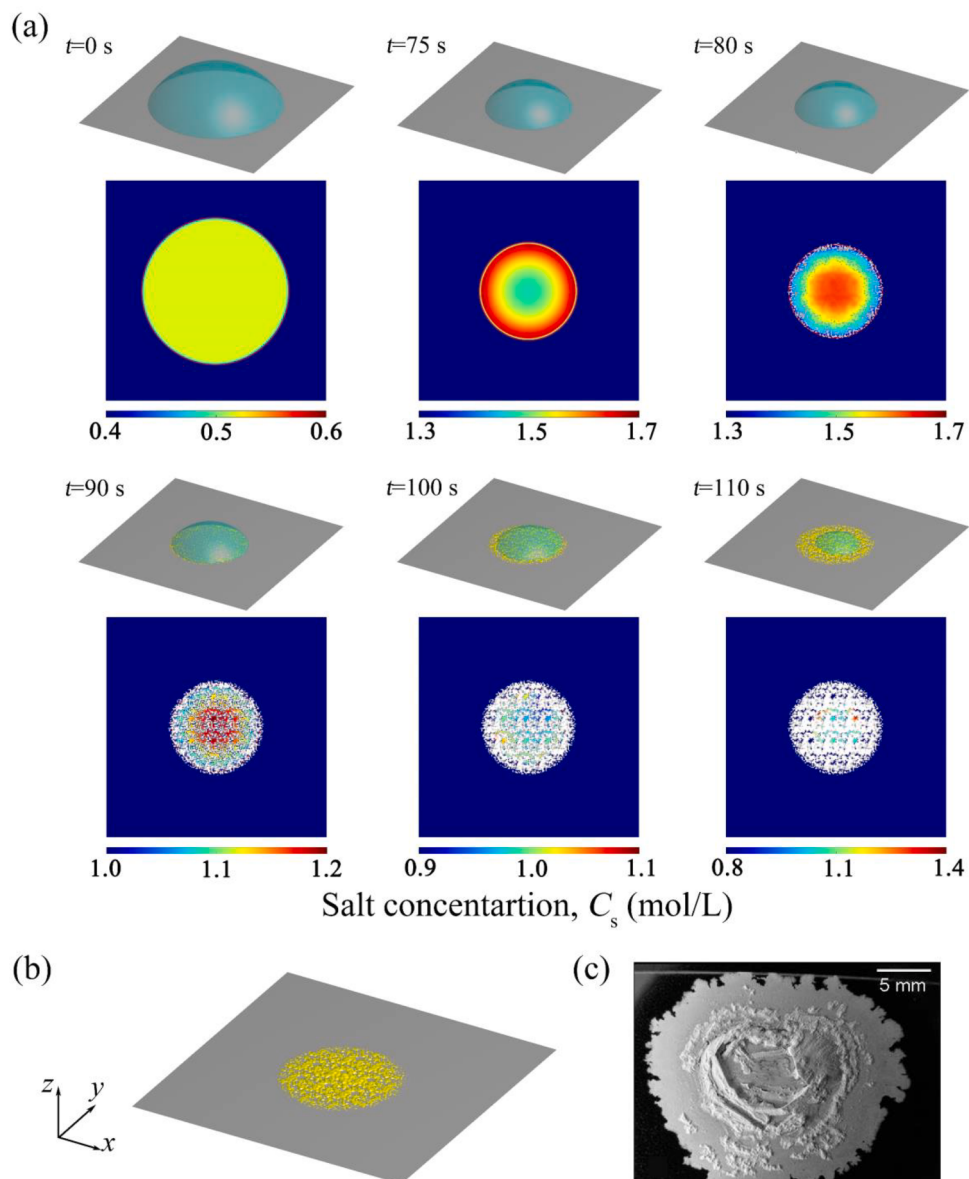


Fig. 9. (a) Numerical results of salt precipitation during brine droplet evaporation with $J_0 = 10^4$, $k = 3.81 \times 10^{-3}\text{mol}/(\text{s} \cdot \text{m}^2)$. (b) Final salt precipitate distribution in the simulation. (c) Previous experimental observation of sodium sulfate precipitation after droplet evaporation (Shahidzadeh-Bonn et al., 2008).

$V_m = 3.69 \times 10^{-5} \text{ m}^3/\text{mol}$ and the nucleation temperature $T_n = 298.15\text{K}$. The parameters for the probability threshold P_{cr} are set as $P_{cr}^{\min} = 0.5$, $P_{cr}^{\max} = 1.5$. Different pre-exponential factors J_0 and kinetic coefficients k are selected in the simulation to investigate the competitive mechanism of nucleation and growth rate.

Fig. 8(a) shows the numerical results with $J_0 = 10^4$, $k = 3.81 \times 10^{-2} \text{ mol}/(\text{s} \cdot \text{m}^2)$, corresponding to the situation where the salt precipitate growth rate is relatively high. As the brine droplet evaporates, the salt concentration increases near the gas–brine interface and diffuses toward the centre of the droplet. At $t = 50\text{s}$, the salt concentration C_s at the interface is almost doubled compared with that at $t = 0\text{s}$, while the concentration inside the droplet is slightly lower. Because of the higher salt concentration, nucleation occurs firstly on the gas–brine interface, as shown at $t = 75\text{s}$. The growth of salt precipitate takes place on the nuclei, resulting in a concentration decrease near the salt surface. Further growth of the salt precipitate continually consumes the salt in brine, inhibiting nucleation at other positions. Only a small amount of nuclei form in the centre of the droplet. At this point, the salt concentration at the droplet centre is slightly higher than the edge, as shown at $t = 90\text{s}$. When $t = 100\text{s}$, salt concentration decreases significantly, and the salt precipitate mainly accumulates on the gas–brine interface, resulting in a ring-like structure. As the droplet continues to shrink, a few scattered salt particles form inside the ring and the salt precipitate structure deforms the brine droplet, which can be found at $t = 110\text{s}$.

The final structure of the salt precipitate in the simulation is presented in Fig. 8(b) with a ring-like shape, which is also observed in previous experiments of sodium chloride precipitation as shown in Fig. 8(c) (Shahidzadeh-Bonn et al., 2008). In the experimental study, this phenomenon was attributed to the ‘coffee-stain effect’ whereby capillary flow brings the homogeneous salt precipitate particles from the

centre to the edge of the droplet. The present work, on the other hand, explains the ring-like structure from the perspective of salt concentration evolution in the heterogeneous nucleation dominated scenario.

Considering that the salt precipitation during brine droplet evaporation is a complicated process including both homogeneous and heterogeneous nucleation and growth, a variety of factors can influence precipitation behaviour. Further clarification of the salt precipitation mechanism requires an extension of the present models to consider more questions such as particle migration (Zhang et al., 2021). Although the present work only focuses on the heterogeneous precipitation, the similarity between experimental and numerical results demonstrates the ability of the proposed models to replicate salt precipitation phenomena in nature, justifying their viability for the application in subsurface engineering where heterogeneous precipitation is dominant.

Salt precipitation with a lower growth rate of $k = 3.81 \times 10^{-3} \text{ mol}/(\text{s} \cdot \text{m}^2)$ is conducted for comparison, as shown in Fig. 9(a). The pre-exponential factor is still $J_0 = 10^4$. The precipitation appears a completely different pattern than that in the high growth rate case of Fig. 8. When $t = 75\text{s}$, no obvious salt particles such as those in Fig. 8(a) have appeared. At this point, nuclei have formed but not grown to a visible size due to the low growth rate. Until $t = 80\text{s}$, nuclei grow to form precipitate particles and distribute the whole droplets. The distribution density of precipitate particles decreases from the droplet edge to the centre. The salt precipitates are more abundant near the gas–brine interface, providing a greater surface area for the salt growth reaction at this location. As a result, more salt is consumed at the droplet edge, resulting in a lower salt concentration compared to the droplet centre. The salt concentration distribution experiences a transition from a high-external-low-internal scheme driven by evaporation ($t = 75\text{s}$) to a low-external-high-internal pattern due to the salt precipitation growth reaction ($t = 80\text{s}$). Because of the higher salt concentration, salt precipitate

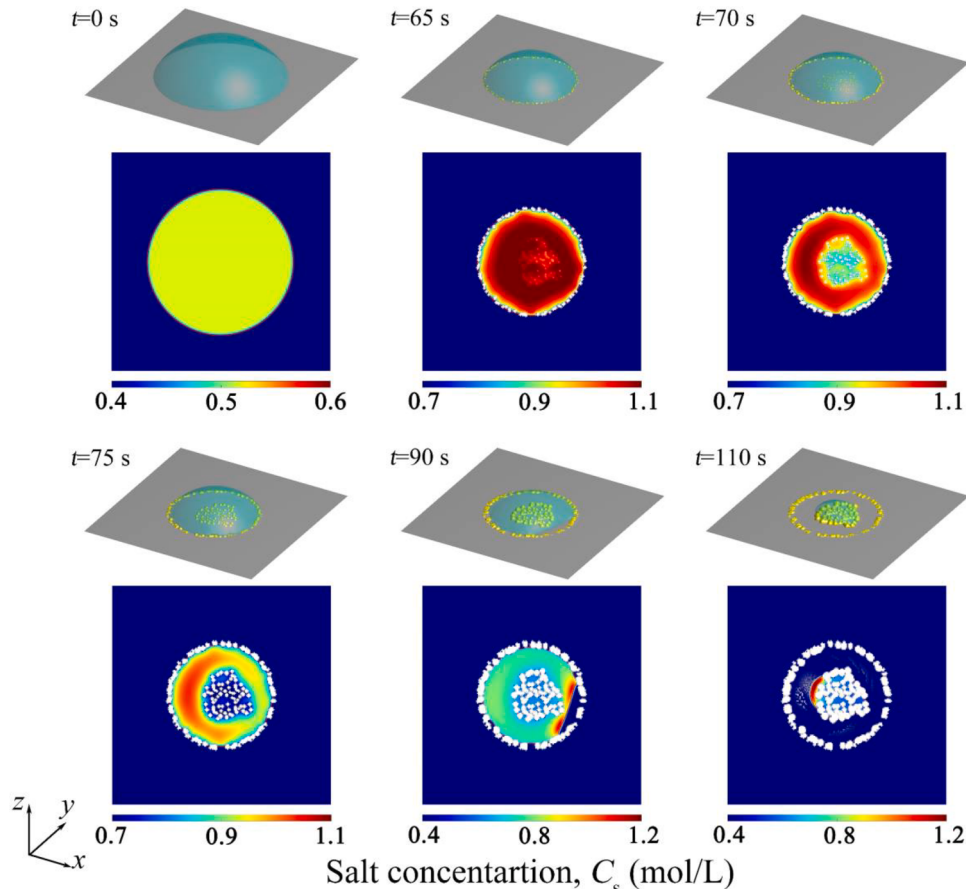


Fig. 10. Numerical results of salt precipitation during brine droplet evaporation with $J_0 = 10^{12}$, $k = 3.81 \times 10^{-2} \text{ mol}/(\text{s} \cdot \text{m}^2)$.

grows more rapidly in the droplet centre at $t = 90\text{s}$, resulting in a uniform salt distribution rather than the ring-like structure. As the droplet shrinks, the salt precipitate only grows below the sites covered by the droplet, leading to a greater amount of salt precipitate accumulated in the centre, as shown at $t = 110\text{s}$. The increasing amount of salt precipitate in the central region finally creates a pancake-like structure as shown in Fig. 9(b), which is similar to the existing experimental observation of sodium sulfate precipitation in Fig. 9(c) (Shahidzadeh-Bonn et al., 2008).

The difference in salt precipitation patterns between Figs. 8 and 9 comes from the competing mechanism between the nucleation and growth reaction. When salt precipitate growth dominates the process, the salt precipitate will grow rapidly after the generation of nuclei, consuming the salt in brine. The rapid growth reaction leads to a violent drop in the salt concentration. For example, from $t = 90\text{s}$ to $t = 100\text{s}$ in Fig. 8(a), the average concentration decreases significantly from 1.5 mol/L to 1.1 mol/L. The salt concentration decrease inhibits nucleation at other positions, thus forming the ring-like structure. By contrast, when nucleation dominates the process, before the salt precipitate has time to grow up, nucleation sites have filled the entire brine droplet, as shown at $t = 80\text{s}$ in Fig. 9(a). From 75 s to 80 s, even though the growth reaction takes place near the edge of the droplet, the salt concentration in the droplet centre is instead rising due to the slow salt consumption rate, thus allowing salt to nucleate at all positions within the droplet. After that, salt precipitation grows uniformly and accumulates obviously in the mid-region as the droplet shrinks, forming a pancake-like structure.

To better understand the competing mechanism between nucleation and growth reaction, the large pre-exponential factor and kinetic coefficient are simultaneously employed in the simulation as $J_0 = 10^{12}$, $k = 3.81 \times 10^{-2}\text{mol}/(\text{s} \cdot \text{m}^2)$. The numerical results of salt precipitation evolution are shown in Fig. 10. Salt precipitate nucleation and growth occur primarily at the edge of the droplet as before at $t = 65\text{s}$. Subsequently, despite the rapid salt growth reaction leading to reduced salt concentration, nucleation still occurs within the droplet interior due to the high nucleation rate at $t = 70\text{s}$. The salt precipitate grows rapidly both at the edge and interior of the droplet, forming a precipitation pattern between the ring-like and pancake-like shapes. By comparing Figs. 8, 9 and 10, we can conclude that the faster nucleation rate results in a more uniform precipitation profile, whereas precipitation becomes more heterogeneous when the growth rate is faster.

This section demonstrates the ability of the present numerical models to simulate typical salt precipitation patterns in nature by comparing with the previous experimental observations (Shahidzadeh-Bonn et al.,

2008). We then apply the numerical models in a microfluidic chip to investigate the effects of salt precipitation in the porous media.

3.4. Salt precipitation in a microfluidic chip

Microfluidic chips are regularly used to study the salt precipitation process during gas injection. This section simulates the salt precipitation process in a microfluidic chip to help gain insights into the experimental phenomenon (Ho and Tsai, 2020). The computational domain is illustrated in Fig. 11. The length and width of the microfluidic chip are $1\text{cm} \times 0.5\text{cm}$ and the height of the flow channel is $80\mu\text{m}$. The circular pillars with a uniform diameter of $d = 500\mu\text{m}$ are arranged in a body-centred lattice to form a porous pattern with porosity $\phi = 0.56$. Initially, some salt-saturated brine remains in the microfluidic chip with a fluid saturation $S_b = 0.22$. A dry gas with $Y_\infty^b \approx 0.001$ is injected from the left inlet to induce brine evaporation, leading to salt precipitation in the microfluidic chip. The fluid densities have the same setting as the previous section, while the viscosities are $\nu_A = 1.0 \times 10^{-6}\text{m}^2/\text{s}$, $\nu_B = 2.0 \times 10^{-7}\text{m}^2/\text{s}$. The diffusion coefficient of the brine vapour $D^b = 3.75 \times 10^{-6}\text{m}^2/\text{s}$ and the gas-brine interfacial tension $\kappa_{bg} \approx 2.8 \times 10^{-6}\text{kg/s}^2$. The contact angle of brine is set as $\theta \approx 30^\circ$ to simulate the hydrophilic microfluidic chip. The solubility product and diffusion coefficient of salt in brine are $K_{sp} = 33.1\text{mol}^2/\text{L}^2$, $D_s = 1.0 \times 10^{-8}\text{m}^2/\text{s}$. The parameters for salt precipitate nucleation and growth are set as $V_m = 3.69 \times 10^{-5}\text{m}^3/\text{mol}$, $J_0 = 10^4$, $P_{cr}^{\min} = 0.5$, $P_{cr}^{\max} = 1.5$, and $k = 3.81 \times 10^{-2}\text{mol}/(\text{s} \cdot \text{m}^2)$ to represent the growth-reaction-dominant situation. The parameters related to salt nucleation and growth can be further fine-tuned based on experimental observations and are not discussed further here. The left inlet of the simulation domain is a pressure boundary where densities of brine and gas are set as $\rho_{in}^b = 0.16\text{kg/m}^3$, $\rho_{in}^g = 208.33\text{kg/m}^3$ (for high injection rate) or $\rho_{in}^g = 120.19\text{kg/m}^3$ (for low injection rate). The right outlet is the outflow boundary (Lou et al., 2013) with a backpressure at the ceiling to ensure fluid drainage. The rest sides of the computational domain are set as solid walls.

By adjusting the inlet pressure, different injection rates are adopted in the simulation to investigate the effect of fluid velocity on the salt precipitation process. The injection rate is characterised by the Péclet number as

$$Pe = \frac{Ud}{D^b} \quad (45)$$

where U is the Darcy velocity in the microfluidic chip. Two typical injection rates are selected as low Pe ($Pe \sim O(10^{-3})$) and high Pe ($Pe \sim O$

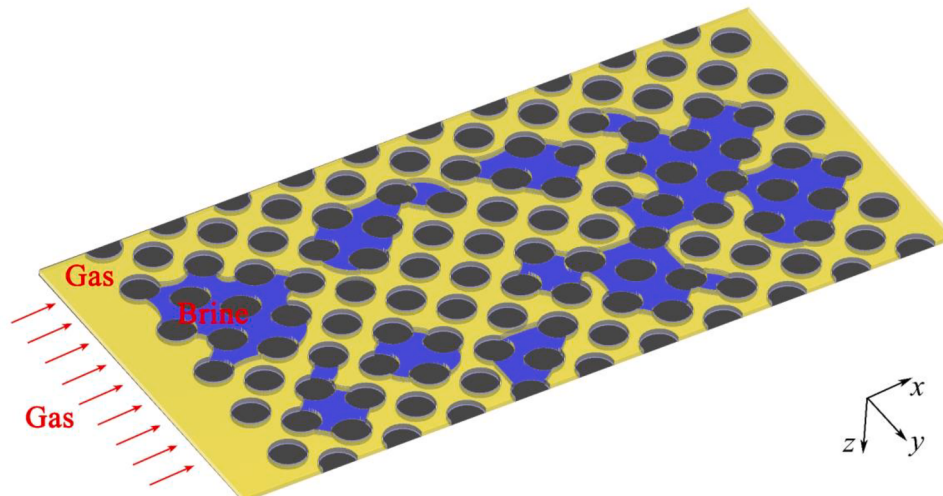


Fig. 11. Computational domain for simulation in the microfluidic chip. The black colour represents the circular pillars in the microfluidic chip. The brine phase is marked in blue and the gas phase is yellow.

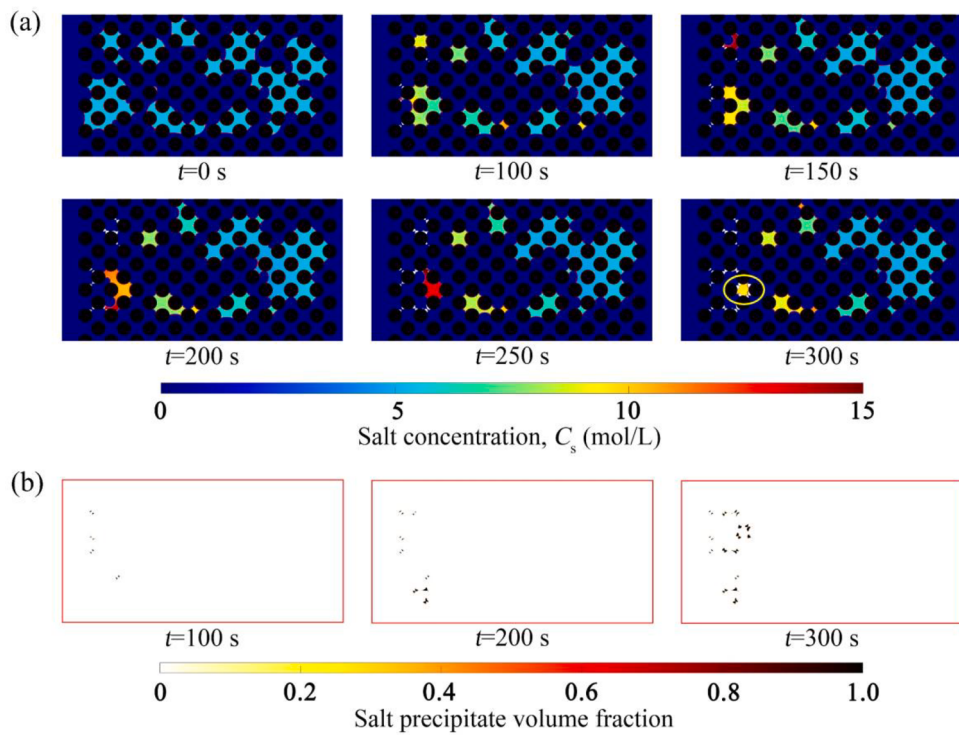


Fig. 12. (a) Numerical results of salt precipitation during gas injection with low injection rate as $\text{Pe} \sim O(10^{-3})$. The contour map illustrates the salt concentration distribution in xy section at $z = 5\mu\text{m}$. The gas-brine interface is marked as red line and the white colour denotes the salt precipitate. (b) Evolution of salt precipitate volume fraction during the precipitation process.

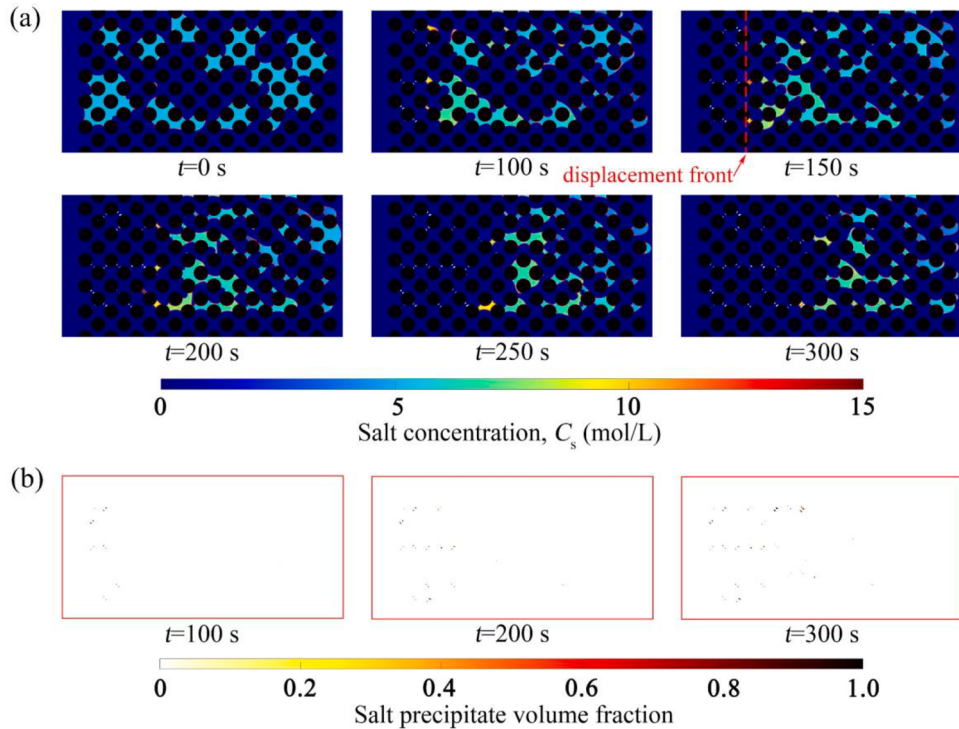


Fig. 13. Numerical results of salt precipitation during gas injection with high injection rate as $\text{Pe} \sim O(10^{-1})$. (b) Evolution of salt precipitate volume fraction during the precipitation process.

(10^{-1})), respectively.

Fig. 12(a) shows the numerical result for the low Pe case. The slowly injected gas cannot displace the brine due to the capillary pressure and the high viscosity ratio (≈ 50), resulting in the brine being almost

immobile and trapped within the chip. In this situation, brine evaporation is primarily driven by the vapour diffusion and the advection effect is negligible. Due to the low mass fraction of brine vapour near the inlet, evaporation of brine occurs primarily in the upstream region. The

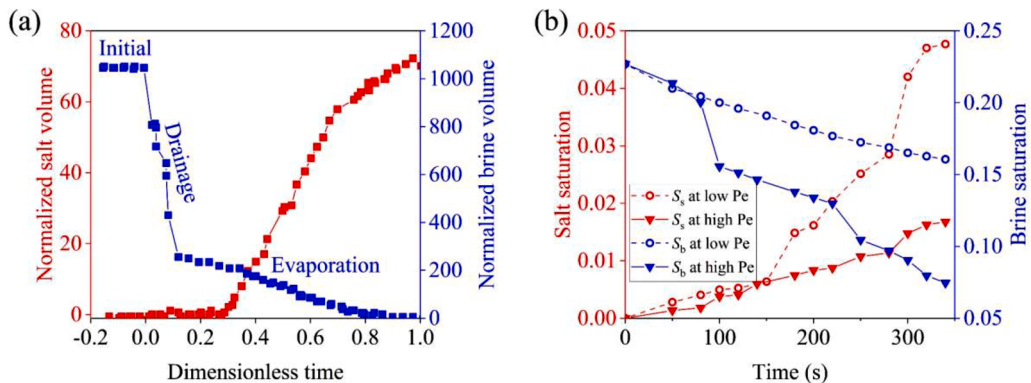


Fig. 14. (a) Salt and brine volume variation curves extracted from the reference experiment results (Ho and Tsai, 2020). (b) Salt and brine saturation variation curves of the numerical results in the present work.

evaporation of the upstream brine causes the salt concentration rise, and thus the salt begins to precipitate as shown in $t = 100$ s. In contrast, the downstream brine is unevaporated, and the salt concentration remains unchanged. As the upstream brine continues to evaporate, the amount of salt precipitate increases and accumulates mainly in the narrow throat channels, as shown from $t = 150$ s to 250 s. The accumulated salt precipitates upstream clog the flow path of the porous media, preventing the injection of gas as well as the diffusion of brine vapour. In some locations, the salt precipitate even encapsulates the residual brine, as marked by the yellow circle at $t = 300$ s, inhibiting the brine evaporation and migration. To underscore the evolution of the salt structure, the distribution of the salt precipitate volume fraction throughout the precipitation process is depicted in Fig. 12(b). It can be observed that salt precipitation predominantly occurs near the inlet side, which can induce substantial obstructions within the pore structure.

The salt precipitation pattern appears quite different when the injection rate is high, as shown in Fig. 13. The stronger inertial force overcomes the capillary pressure and displaces the brine out of the chip. During the displacement, some large brine clusters fragment into scattered droplets by the pore structure. With the continuous injection of dry air, the scattered droplets near the inlet evaporate at first, leading to an increase in the salt concentration, as shown in $t = 100$ s. A few particles of salt precipitate are generated near the inlet but do not continue to grow up because brine droplets are displaced to leave the area. Hereafter, the displacement front moves steadily forward, and the brine evaporation mainly occurs near the displacement front, resulting in a higher salt concentration there. As a result, salt precipitation preferentially occurs at the vicinity of the displacement front and remains in a

Table 2

Permeability of the microfluidic chip with salt precipitation at $t = 300$ s.

	Low Pe	High Pe
Permeability (μm^2)	116	125
Permeability degradation rate	8.7 %	1.7 %

dispersion pattern behind the displacement front as it advances from $t = 150$ s to 300 s. Compared to the low Pe case, the salt precipitation is more evenly distributed in the chip with smaller particle size as shown in Fig. 13(b), and hence a relatively weaker clogging effect on the porous structure.

According to existing experimental observations during the gas injection in a microfluidic chip (Ho and Tsai, 2020), there are three sequential states of brine de-wetting, including the initial full brine saturation, drainage, and evaporation of residual brine, as shown in Fig. 14(a). To compare with these experimental results, Fig. 14(b) plots the variation of salt saturation S_s and brine saturation S_b for quantitative analysis. Numerical results from the low Pe case show that brine saturation S_b decreases smoothly at a steady rate due to the diffusion-controlled evaporation. At the same time, the salt saturation S_s follows a two-stage path, with an initial slow increase before 150 s followed by a rapid growth after 150 s. The first stage corresponds to the nucleation and initial nucleus growth of salt precipitate, while the rapid growth of the second stage results from the salt concentration increase and the expansion of the salt surface area. The evolution pattern of S_s and S_b exhibits a consistent trend with the third state in the experimental observation, i.e., the evaporation of residual brine. At this state, both numerically and experimentally, brine is trapped in the chip and de-wetting of the brine is achieved primarily by evaporation. When Pe is high, the brine saturation S_b is significantly reduced due to the displacement of the injected gas. As the salt precipitate growth reaction occurs only in the location covered by brine, the continuous migration of brine limits the further growth of the salt precipitate particles. Consequently, the growth rate of salt saturation S_s is relatively slow. The evolution of salt and brine saturation is similar to the second state in the experiment where drainage is the major form of brine de-wetting. The consistency between the experimental and numerical results demonstrates that the proposed numerical models can reliably simulate the salt precipitation process in porous media under different conditions.

To evaluate the effect of salt precipitation at different injection rates, Fig. 15 tracks the distribution of salt precipitate along x -axis by integrating salt volume V_s over each yz section at $t = 300$ s. When the injection rate is slow (low Pe), salt precipitate predominantly accumulates in the upstream region at $x = 2$ mm. The deposition of salt precipitate leads to the blockage of the upstream pore structure, impairing the reservoir permeability and inhibiting further gas injection, as illustrated in Fig. 12. For higher injection rate, salt precipitates uniformly

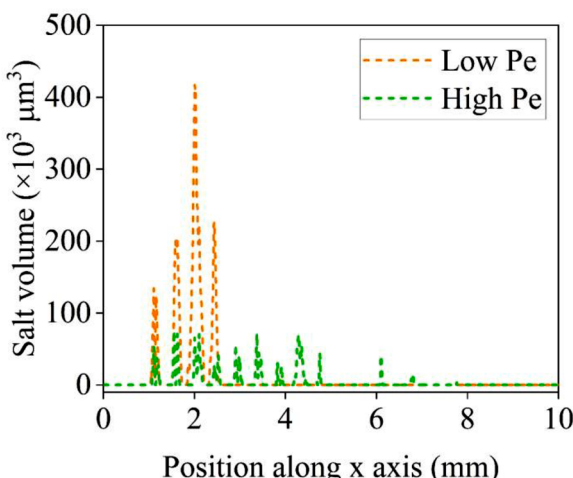


Fig. 15. Salt precipitate distribution along x -axis at $t = 300$ s.

distributed along the x -axis in a pint-sized pattern. The fragmented salt precipitate is less detrimental to reservoir permeability and therefore the brine can be continuously displaced, as shown in Fig. 13. To quantify the effect of salt precipitation, the permeability of the microfluidic chip with salt precipitate K is calculated in Table 2. The primary permeability of the microfluidic chip without salt precipitate is $K_0 = 127\mu\text{m}^2$ and the permeability degradation rate is calculated by $1 - K/K_0$. At low Pe, the permeability decreases by almost 10 % with a salt saturation less than 5 %, indicating the blockage of salt precipitate is significant. When the injection rate is high, less salt precipitation is produced with a more uniform distribution, resulting in a smaller impact on the permeability of the pore structure.

The above analysis suggests that a higher injection rate is conducive to improving the reservoir injectivity, which provides some guidance for engineering scenarios such as CO_2 sequestration. Finally, it should be noted that the practical gas injection process is complex and has other influential factors, including reservoir structure, wettability, and brine evaporation rate. Further simulations are required to understand the impact of these factors comprehensively.

4. Conclusions

In this work, numerical models for salt precipitation during brine evaporation are proposed based on the lattice Boltzmann framework. A multiphase multicomponent pseudopotential model is used to simulate brine evaporation by introducing both intercomponent and intra-component forces. The mass transfer of brine vapour in the gas phase is described by the advection-diffusion Eq. (18) and the parameter settings for the diffusion coefficient are conveniently obtained by the Stefan problem. Salt concentration is computed by the CST-LB model and salt mass conservation at the gas–brine interface is verified. The nucleation of salt precipitate is determined by the classical nucleation theory and the salt precipitate growth is treated as a heterogeneous reaction. The numerical models are available to simulate the salt concentration increase and the salt precipitation due to the brine evaporation.

Following the construction of the lattice Boltzmann models, salt precipitation during brine droplet evaporation is simulated to investigate the competitive mechanism between salt precipitate nucleation and growth reaction. When the growth reaction dominates the precipitation process, the salt precipitate preferentially grows near the gas–brine interface, forming a ring-like precipitation structure. When the nucleation rate is more rapid, the salt precipitate can nucleate and grow across the whole range of locations inside the droplet. With the shrinking of the droplet, the salt precipitate eventually forms a pancake-like pattern. The final structure of salt precipitate in the numerical results shows consistency with the typical patterns in existing experimental observations, indicating the proposed models are able to reproduce the salt precipitation process in nature.

Furthermore, we simulate the salt precipitation during gas injection in the microfluidic chip with different injection rates. The evolution trends of salt and brine saturation are consistent with previous experimental results. When the injection rate is low ($\text{Pe} \sim O(10^{-3})$), the injected gas is unable to remove the brine trapped in the pore structure. Brine evaporation occurs primarily in the upstream area near the inlet via brine vapour diffusion. The high salt concentration in the upstream brine causes salt precipitate to accumulate near the inlet. The salt precipitates preferentially grow in the narrow throat, which is detrimental to the permeability of the pore structure. For the high injection rate ($\text{Pe} \sim O(10^{-1})$), the brine is displaced from the chip by the injected gas and the brine evaporation occurs on the displacement front. Due to the migration of brine, salt precipitates are difficult to grow and uniformly distributed in the scattered pattern, which has less impact on reservoir permeability. In the future, we plan to apply the developed models to more complicated pore structures to investigate the influence of additional parameters and pore structures on salt precipitation events, which may provide guidance for practical engineering scenarios like CO_2

sequestration. We will also improve the physical models to consider more complicated precipitation phenomena in nature, such as anisotropic crystallisation, precipitate migration and wettability change due to the salt precipitation.

CRediT authorship contribution statement

Junyu Yang: Conceptualization, Methodology, Software, Validation, Formal analysis, Investigation, Writing – original draft, Visualization. **Timan Lei:** Methodology, Investigation, Writing – review & editing. **Geng Wang:** Methodology, Investigation, Writing – review & editing. **Qianghui Xu:** Investigation, Data curation, Writing – review & editing. **Jin Chen:** Methodology, Investigation. **Kai H. Luo:** Supervision, Project administration, Funding acquisition, Writing – review & editing.

Declaration of Competing Interest

The authors declare that they have no known competing financial interests or personal relationships that could have appeared to influence the work reported in this paper.

Data availability

Data will be made available on request.

Acknowledgements

The research is supported by the UK Engineering and Physical Sciences Research Council (EPSRC) under the grant No. EP/W026260/1. ARCHER2 supercomputing resources provided by the EPSRC project “UK Consortium on Mesoscale Engineering Sciences (UKCOMES)” (Grant No. EP/X035875/1) are gratefully acknowledged. This work made use of computational support by CoSeC, the Computational Science Centre for Research Communities, through UKCOMES.

References

- Akindipe, D., Saraji, S., Piri, M., 2021. Salt precipitation during geological sequestration of supercritical CO_2 in saline aquifers: a pore-scale experimental investigation. *Adv. Water Resour.* 155, 104011.
- Akindipe, D., Saraji, S., Piri, M., 2022. Salt precipitation in carbonates during supercritical CO_2 injection: a pore-scale experimental investigation of the effects of wettability and heterogeneity. *Int. J. Greenh. Gas Control* 121, 103790.
- Borgia, A., Pruess, K., Kneafsey, T.J., Oldenburg, C.M., Pan, L., 2012. Numerical simulation of salt precipitation in the fractures of a CO_2 -enhanced geothermal system. *Geothermics* 44, 13–22.
- Chai, Z.-H., Zhao, T.-S., 2012. A pseudopotential-based multiple-relaxation-time lattice Boltzmann model for multicomponent/multiphase flows. *Acta Mech. Sin.* 28, 983–992.
- Chen, L., Kang, Q., Carey, B., Tao, W.-Q., 2014. Pore-scale study of diffusion-reaction processes involving dissolution and precipitation using the lattice Boltzmann method. *Int. J. Heat. Mass Transf.* 75, 483–496.
- Chen, L., Zhang, R., Kang, Q., Tao, W.Q., 2020. Pore-scale study of pore-ionomer interfacial reactive transport processes in proton exchange membrane fuel cell catalyst layer. *Chem. Eng. J.* 391, 123590.
- Dashtian, H., Shokri, N., Sahimi, M., 2018. Pore-network model of evaporation-induced salt precipitation in porous media: the effect of correlations and heterogeneity. *Adv. Water Resour.* 112, 59–71.
- Deng, H., Gharasooi, M., Zhang, L., Dai, Z., Hajizadeh, A., Peters, C.A., Soulaine, C., Thullner, M., Van Cappellen, P., 2022a. A perspective on applied geochemistry in porous media: reactive transport modeling of geochemical dynamics and the interplay with flow phenomena and physical alteration. *Appl. Geochem.* 146, 105445.
- Deng, H., Poonoosamy, J., Molins, S., 2022b. A reactive transport modeling perspective on the dynamics of interface-coupled dissolution-precipitation. *Appl. Geochem.* 137, 105207.
- Espinosa-Marzal, R.M., Scherer, G.W., 2010. Advances in understanding damage by salt crystallization. *Acc. Chem. Res.* 43, 897–905.
- Espinosa-Marzal, R.M., Scherer, G.W., 2022. Mechanisms of damage by salt. *Geol. Soc., Lond., Special Publ.* 331, 61–77.
- Fazeli, H., Masoudi, M., Patel, R.A., Aagaard, P., Hellevang, H., 2020. Pore-scale modeling of nucleation and growth in porous media. *ACS Earth Space Chem.* 4, 249–260.

- Fei, L., Du, J., Luo, K.H., Succi, S., Lauricella, M., Montessori, A., Wang, Q., 2019. Modeling realistic multiphase flows using a non-orthogonal multiple-relaxation-time lattice Boltzmann method. *Phys. Fluids* 31, 042105.
- Flatt, R.J., Caruso, F., Sanchez, A.M., Scherer, G.W., 2014. Chemo-mechanics of salt damage in stone. *Nat. Commun.* 5, 4823.
- Flekkøy, E.G., 1993. Lattice Bhatnagar-Gross-Krook models for miscible fluids. *Phys. Rev. E* 47, 4247–4257.
- Fonseca, P.C., Scherer, G.W., 2014. An image analysis procedure to quantify the air void system of mortar and concrete. *Mater. Struct.* 48, 3087–3098.
- Fujii, T., Kawasaki, S.-i., 2019. Salting-out effects on vanillin extraction by supercritical carbon dioxide from aqueous vanillin solution containing salts. *J. Supercrit. Fluids* 152, 104550.
- Graveleau, M., Soulaine, C., Tchelepi, H.A., 2017. Pore-scale simulation of interphase multicomponent mass transfer for subsurface flow. *Transp. Porous Media* 120, 287–308.
- Gunstensen, A.K., Rothman, D.H., Zaleski, S., Zanetti, G., 1991. Lattice Boltzmann model of immiscible fluids. *Phys. Rev. A* 43, 4320–4327.
- Guo, G., Zhang, P., Lei, L., Galindo-Torres, S.A., 2022. A pseudopotential lattice Boltzmann model for simulating mass transfer around a rising bubble under real buoyancy effect. *Phys. Fluids* 34, 083306.
- Guo, Z., Zheng, C., 2008. Analysis of lattice Boltzmann equation for microscale gas flows: relaxation times, boundary conditions and the Knudsen layer. *Int. J. Comput. Fluid Dyn.* 22, 465–473.
- Han, Y., Wang, Q., Liu, J., Xia, W., Wang, J., Shen, J., Chen, Y., 2022. Pore-scale study on the characteristic hydraulic conductivity of a dispersive lean clay affected by salinity and freeze-thaw. *Bull. Eng. Geol. Environ.* 81, 107.
- Haroun, Y., Legendre, D., Raynal, L., 2010. Volume of fluid method for interfacial reactive mass transfer: application to stable liquid film. *Chem. Eng. Sci.* 65, 2896–2909.
- He, D., Jiang, P., Xu, R., 2019. Pore-scale experimental investigation of the effect of supercritical CO₂ injection rate and surface wettability on salt precipitation. *Environ. Sci. Technol.* 53, 14744–14751.
- He, D., Xu, R., Ji, T., Jiang, P., 2022. Experimental investigation of the mechanism of salt precipitation in the fracture during CO₂ geological sequestration. *Int. J. Greenh. Gas Control* 118, 103693.
- He, X., Chen, S., Zhang, R., 1999. A lattice Boltzmann scheme for incompressible multiphase flow and its application in simulation of Rayleigh–Taylor instability. *J. Comput. Phys.* 152, 642–663.
- Ho, T.M., Tsai, P.A., 2020. Microfluidic salt precipitation: implications for geological CO₂ storage. *Lab Chip* 20, 3806–3814.
- Kim, M., Sell, A., Sinton, D., 2013. Aquifer-on-a-chip: understanding pore-scale salt precipitation dynamics during CO₂ sequestration. *Lab Chip* 13, 2508–2518.
- Kohanpur, A.H., Rahromostaqim, M., Valocchi, A.J., Sahimi, M., 2020. Two-phase flow of CO₂-brine in a heterogeneous sandstone: characterization of the rock and comparison of the lattice-Boltzmann, pore-network, and direct numerical simulation methods. *Adv. Water Resour.* 135, 103469.
- Latt, J., Malaspinas, O., Kontaxakis, D., Parmigiani, A., Lagrava, D., Brogi, F., Belgacem, M.B., Thorimbert, Y., Leclaire, S., Li, S., Marson, F., Lemus, J., Kotsalos, C., Conradin, R., Coreixas, C., Petkanitch, R., Raynaud, F., Beny, J., Chopard, B., 2021. Palabos: parallel lattice Boltzmann solver. *Comput. Math. Appl.* 81, 334–350.
- Li, Q., Fernandez-Martinez, A., Lee, B., Waychunas, G.A., Jun, Y.S., 2014. Interfacial energies for heterogeneous nucleation of calcium carbonate on mica and quartz. *Environ. Sci. Technol.* 48, 5745–5753.
- Li, Q., Luo, K.H., Kang, Q.J., He, Y.L., Chen, Q., Liu, Q., 2016. Lattice Boltzmann methods for multiphase flow and phase-change heat transfer. *Prog. Energy Combust. Sci.* 52, 62–105.
- Li, Q., Luo, K.H., Li, X.J., 2013. Lattice Boltzmann modeling of multiphase flows at large density ratio with an improved pseudopotential model. *Phys. Rev. E* 87, 053301.
- Liu, Q., Guo, Z., Shi, B., 2013. Evaluation of outflow boundary conditions for two-phase lattice Boltzmann equation. *Phys. Rev. E Stat. Nonlinear Soft Matter Phys.* 87, 063301.
- Masoudi, M., Fazeli, H., Miri, R., Hellevang, H., 2021. Pore scale modeling and evaluation of clogging behavior of salt crystal aggregates in CO₂-rich phase during carbon storage. *Int. J. Greenh. Gas Control* 111, 103475.
- Miri, R., van Noort, R., Aagaard, P., Hellevang, H., 2015. New insights on the physics of salt precipitation during injection of CO₂ into saline aquifers. *Int. J. Greenh. Gas Control* 43, 10–21.
- Mukherjee, S., Berghout, P., Van den Akker, H.E.A., 2019. A lattice Boltzmann approach to surfactant-laden emulsions. *AIChE J.* 65, 811–828.
- Nachshon, U., Shahraeeni, E., Or, D., Dragila, M., Weisbrod, N., 2011. Infrared thermography of evaporative fluxes and dynamics of salt deposition on heterogeneous porous surfaces. *Water Resour. Res.* 47, W12519.
- Newman, J., Balsara, N.P., 2021. Electrochemical Systems. John Wiley & Sons.
- Nooraeipour, M., Masoudi, M., Hellevang, H., 2021a. Probabilistic nucleation governs time, amount, and location of mineral precipitation and geometry evolution in the porous medium. *Sci. Rep.* 11, 16397.
- Nooraeipour, M., Masoudi, M., Shokri, N., Hellevang, H., 2021b. Probabilistic nucleation and crystal growth in porous medium: new insights from calcium carbonate precipitation on primary and secondary substrates. *ACS Omega* 6, 28072–28083.
- Norouzi Rad, M., Shokri, N., Sahimi, M., 2013. Pore-scale dynamics of salt precipitation in drying porous media. *Phys. Rev. E Stat. Nonlinear Soft Matter Phys.* 88, 032404.
- Oh, J., Kim, K.-Y., Han, W.S., Kim, T., Kim, J.-C., Park, E., 2013. Experimental and numerical study on supercritical CO₂/brine transport in a fractured rock: implications of mass transfer, capillary pressure and storage capacity. *Adv. Water Resour.* 62, 442–453.
- Ott, H., Roels, S.M., de Kloet, K., 2015. Salt precipitation due to supercritical gas injection: I. Capillary-driven flow in unimodal sandstone. *Int. J. Greenh. Gas Control* 43, 247–255.
- Peng, C., Tian, S., Li, G., Sukop, M.C., 2019. Simulation of multiple cavitation bubbles interaction with single-component multiphase Lattice Boltzmann method. *Int. J. Heat Mass Transf.* 137, 301–317.
- Prasianakis, N.I., Curti, E., Kosakowski, G., Poonoosamy, J., Churakov, S.V., 2017. Deciphering pore-level precipitation mechanisms. *Sci. Rep.* 7, 13765.
- Rad, M.N., Shokri, N., Keshmiri, A., Withers, P.J., 2015. Effects of grain and pore size on salt precipitation during evaporation from porous media. *Transp. Porous Media* 110, 281–294.
- Rahimi, A., Kasaeipoor, A., Hasani Malekshah, E., Rashidi, M.M., Purusothaman, A., 2019. Lattice Boltzmann simulation of 3D natural convection in a cuboid filled with KKL-model predicted nanofluid using dual-MRT model. *Int. J. Numer. Methods Heat Fluid Flow* 29, 365–387.
- Roels, S.M., Ott, H., Zitha, P.L.J., 2014. μ -CT analysis and numerical simulation of drying effects of CO₂ injection into brine-saturated porous media. *Int. J. Greenh. Gas Control* 27, 146–154.
- Saxena, N., Hofmann, R., Alpk, F.O., Berg, S., Dietderich, J., Agarwal, U., Tandon, K., Hunter, S., Freeman, J., Wilson, O.B., 2017. References and benchmarks for pore-scale flow simulated using micro-CT images of porous media and digital rocks. *Adv. Water Resour.* 109, 211–235.
- Shahidzadeh-Bonn, N., Rafai, S., Bonn, D., Wegdam, G., 2008. Salt crystallization during evaporation: impact of interfacial properties. *Langmuir* 24, 8599–8605.
- Shan, X., Chen, H., 1993. Lattice Boltzmann model for simulating flows with multiple phases and components. *Phys. Rev. E* 47, 1815–1819.
- Shan, X., Doolen, G., 1995. Multicomponent lattice-Boltzmann model with interparticle interaction. *J. Stat. Phys.* 81, 379–393.
- Shokri-Kuehni, S.M.S., Raaijmakers, B., Kurz, T., Or, D., Helmig, R., Shokri, N., 2020. Water table depth and soil salinization: from pore-scale processes to field-scale responses. *Water Resour. Res.* 56, e2019WR026707.
- Shokri, N., 2014. Pore-scale dynamics of salt transport and distribution in drying porous media. *Phys. Fluids* 26, 012106.
- Sokama-Neuyam, Y.A., Ursin, J.R., Boakye, P., 2019. Experimental investigation of the mechanisms of salt precipitation during CO₂ injection in sandstone. *C – J. Carbon Res.* 5, 4.
- Starchenko, V., 2022. Pore-scale modeling of mineral growth and nucleation in reactive flow. *Front. Water* 3, 800944.
- Stephen, R.T., 2000. An Introduction to combustion: Concepts and Applications. McGraw-Hill Companies, Inc.
- Sullivan, S.P., Sani, F.M., Johns, M.L., Gladden, L.F., 2005. Simulation of packed bed reactors using lattice Boltzmann methods. *Chem. Eng. Sci.* 60, 3405–3418.
- Swift, M.R., Orlandini, E., Osborn, W., Yeomans, J., 1996. Lattice Boltzmann simulations of liquid-gas and binary fluid systems. *Phys. Rev. E* 54, 5041.
- Tambach, T.J., Loeve, D., Hofstee, C., Plug, W.-J., Maas, J.G., 2014. Effect of CO₂ injection on brine flow and salt precipitation after gas field production. *Transp. Porous Media* 108, 171–183.
- Wang, G., Fei, L., Luo, K.H., 2022. Unified lattice Boltzmann method with improved schemes for multiphase flow simulation: application to droplet dynamics under realistic conditions. *Phys. Rev. E* 105, 045314.
- Yang, J., Dai, X., Xu, Q., Liu, Z., Shi, L., 2022. Comparative investigation of a lattice Boltzmann boundary treatment of multiphase mass transport with heterogeneous chemical reactions. *Phys. Rev. E* 105, 055302.
- Yang, J., Dai, X., Xu, Q., Liu, Z., Shi, L., Long, W., 2021. Lattice Boltzmann modeling of interfacial mass transfer in a multiphase system. *Phys. Rev. E* 104, 015307.
- Yang, X., Mehmani, Y., Perkins, W.A., Pasquali, A., Schönher, M., Kim, K., Perego, M., Parks, M.L., Trask, N., Balhoff, M.T., Richmond, M.C., Geier, M., Krafczyk, M., Luo, L.-S., Tartakovsky, A.M., Scheibe, T.D., 2016. Intercomparison of 3D pore-scale flow and solute transport simulation methods. *Adv. Water Resour.* 95, 176–189.
- Yoon, H., Valocchi, A.J., Werth, C.J., Dewers, T., 2012. Pore-scale simulation of mixing-induced calcium carbonate precipitation and dissolution in a microfluidic pore network. *Water Resour. Res.* 48, W02524.
- Yuan, P., Schaefer, L., 2006. Equations of state in a lattice Boltzmann model. *Phys. Fluids* 18, 042101.
- Zhang, C., Zhang, H., Zhao, Y., Yang, C., 2021. An immersed boundary-lattice Boltzmann model for simulation of deposited particle patterns in an evaporating sessile droplet with dispersed particles. *Int. J. Heat Mass Transf.* 181, 121905.
- Zhang, L., Wang, R., 2012. Salting-out effect on facilitated transport membranes for CO₂ separation: from fluoride salt to polyoxometalates. *RSC Adv.* 2, 9551–9554.
- Zhaoyong, Z., Abuduwalli, J., Yimit, H., 2014. The occurrence, sources and spatial characteristics of soil salt and assessment of soil salinization risk in Yanqi basin, northwest China. *PLoS One* 9, e106079.
- Zhou, P., Liu, W., Liu, Z., 2019. Lattice Boltzmann simulation of nucleate boiling in micro-pillar structured surface. *Int. J. Heat Mass Transf.* 131, 1–10.